Available online at www.sciencedirect.com
SCIENCE DIRECT®
Journal of Magnetic Resonance 173 (2005) 259–279
JMR Journal of Magnetic Resonance
www.elsevier.com/locate/jmr

# Triple-quantum dynamics in multiple-spin systems undergoing magic-angle spinning: application to $^{13}C$ homonuclear correlation spectroscopy

Mattias Edén[a,*], Andreas Brinkmann[b]

[a] *Physical Chemistry Division, Arrhenius Laboratory, Stockholm University, SE-106 91 Stockholm, Sweden*
[b] *Solid State NMR, Radboud University Nijmegen, 6525 ED Nijmegen, The Netherlands*

Received 8 October 2004; revised 15 December 2004
Available online 1 February 2005

**Abstract**

We analyze the multiple-quantum dynamics governed by a new homonuclear recoupling strategy effecting an average dipolar Hamiltonian comprising three-spin triple-quantum operators (e.g., $S_p^+ S_q^+ S_r^+$) under magic-angle spinning conditions. Analytical expressions are presented for polarization transfer processes in systems of three and four coupled spins-1/2 subject to triple-quantum filtration (3QF), and high-order multiple-quantum excitation is investigated numerically in moderately large clusters, comprising up to seven spins. This recoupling approach gives highly efficient excitation of triple-quantum coherences: ideally, up to 67% of the initial polarization may be recovered by 3QF in three-spin systems in polycrystalline powders. Two homonuclear 2D correlation strategies are demonstrated experimentally on powders of uniformly $^{13}C$-labeled alanine and tyrosine: the first correlates the single-quantum spectrum in the first dimension with the corresponding 3QF spectrum along the other. The second protocol correlates triple-quantum coherences with their corresponding single-quantum coherences within triplets of coupled spins.


*Keywords:* Multiple-quantum coherence; 3Q recoupling; Magic-angle-spinning; Symmetry-based pulse sequences

## 1. Introduction

Multiple-quantum coherences (MQC) have found widespread use in solid state NMR for spectral editing purposes and for probing molecular structure, such as measuring internuclear distances and molecular torsion angles [1–3]. MQC may only develop in systems of coupled spins, where in this work we consider the through-space dipolar interaction. Creating MQC requires application of radio-frequency (RF) pulse sequences effecting suitable effective Hamiltonians. Hitherto, the most exploited pulse schemes in static solids effect either two-spin 1Q dipolar Hamiltonians [4] comprising operators of the type $S_p^+ S_{qz}$, or 2Q operators of the form $S_p^+ S_q^+$ [5–8]. Such sequences will be referred to as providing 1Q and 2Q recoupling, respectively. As the highest excitable coherence order in a spin cluster equals the number of coupled spins-1/2 therein, techniques for optimal excitation of MQC have been developed in static solids for determining cluster sizes and their topologies. Consequently, the MQC dynamics resulting from 1Q or 2Q effective dipolar Hamiltonians have received considerable attention by theoretical, numerical, and experimental studies [1,4–14].

However, as the dipolar interactions are averaged out by magic-angle spinning (MAS), high-resolution solid state NMR requires rotor-synchronized recoupling sequences to provide dipolar Hamiltonians involving multiple-quantum operators. To date, many 2Q recoupling techniques exist [15]. Unfortunately, the generation of MQC in powders under MAS conditions is much less

* Corresponding author. Fax: +46 8 152187.
*E-mail address:* mattias@physc.su.se (M. Edén).

1090-7807/$ - see front matter © 2005 Elsevier Inc. All rights reserved.
doi:10.1016/j.jmr.2004.12.008

efficient than in static samples, in particular for coherence orders higher than two. As a result, the excitation of high-order coherences have found comparatively little attention in MAS NMR. Nevertheless, 3QC have been useful for spin counting [16] and estimating peptide torsion angles [17] and dynamic order parameters in elastomers [18]. Further methodological and theoretical developments are therefore needed to remedy the difficulties in high-order MQC excitation under MAS conditions. As a dent towards this solution, we have recently demonstrated a new strategy for reintroducing MAS-averaged interactions in a systematic manner [19,20], based on symmetry-based $CN_n^v$ and $RN_n^v$ pulse sequences [21] in conjunction with average Hamiltonian theory (AHT) [22,23]. This approach builds on concepts introduced for MQC excitation in static samples [24] but differs from previous homonuclear recoupling strategies under MAS conditions, in that the desired average Hamiltonian arise from commutators (usually called "cross-terms") between operators from two spin interactions. This approach is referred to as *second-order recoupling* [19,20,25]. It makes it feasible to obtain more complex Hamiltonian terms than the one- or two-spin operators normally encountered in the high-field spin Hamiltonian, or any average Hamiltonian derived thereof to lowest (i.e., first) order.

Focusing on 3Q dipolar recoupling, we have presented second-order recoupling schemes leading to homonuclear dipolar cross-terms comprising three-spin 3Q operators (e.g., $S_p^+S_q^+S_r^+$) [19,20]. We have experimentally demonstrated $^1$H [19] and $^{13}$C [20] 3QC excitation in organic molecules. The purpose of the present article is to analyze the dynamics generated by a 3Q Hamiltonian, with particular focus on the mechanism and efficiency of 3QC excitation in multiple-spin systems, polarization-transfer processes between spins subject to a 3Q Hamiltonian, as well as the potential of obtaining structural parameters through triple-quantum filtration (3QF) experiments. This treatment thus parallels previous MQC analyses carried out for two-spin 1Q and 2Q Hamiltonians [4–6,8,9,12].

Two homonuclear 2D correlation strategies incorporating 3QF are demonstrated experimentally on powders of uniformly $^{13}$C-labeled alanine and tyrosine. The first is a NOESY-type experiment [26] that correlates 1QC along each spectral dimension. The second protocol correlates triple-quantum coherences with their corresponding single-quantum coherences within triplets of coupled spins, and may be viewed as a 3QC analog of the 2Q INADEQUATE experiment [27], also implemented in solid state NMR [28–31]. The pulse schemes are introduced and demonstrated on alanine in the following section, and results on tyrosine are discussed in Section 9. Appendix A reviews restrictions that apply when using second-order recoupling pulse sequences within 2D experiments.

We outline the general strategy for generating a pure 3Q average Hamiltonian in Section 3, and demonstrate in Sections 4–6 that its resulting 3QC dynamics may be solved exactly in three- and four-spin systems. These expressions give 3QF amplitudes as function of the excitation interval (i.e., the duration over which recoupling is effected), involve the dipolar couplings within the system, and provide insight into general 3QC excitation trends. Sections 7 and 8 present numerical AHT calculations of the buildup of 3QC and higher-order MQC in systems of six and seven spins, initially prepared either with longitudinal or transverse polarization.

Nevertheless, our analysis is somewhat pragmatic; despite that in some cases it is possible to effect such ideal 3Q average Hamiltonians using supercycled pulse sequences [20], in general, the MQC dynamics of the sequences considered here is governed by a mixture of three-spin 3Q and zero-quantum (ZQ) Hamiltonian terms, leading to less tractable spin dynamics, that are generally not exactly solvable. The combined effects of 3Q and ZQ average Hamiltonians were briefly considered by numerical simulations of three-spin systems in [20], and will be discussed further here within the framework of 2D correlation spectroscopy in multiple-spin systems.

## 2. Pulse schemes

### 2.1. 3Q dipolar recoupling sequences

We focus particularly on the 3Q recoupling scheme $(R18_3^7)3^1$ that belong to the class of *symmetry-based 3Q phase-cycles*, denoted $(RN_n^v)3^1$ [19,20]. Such a sequence is formed from an $RN_n^v$ cycle [21,32,33], in turn constructed from a composite π-pulse element $\mathcal{R}$. In this work we employ the windowed element [20,34]

$$\mathcal{R}(\beta) = \{\beta_0 - \tau_w - \pi_0 - \tau_w - \beta_\pi\}. \quad (1)$$

The flip angle $\beta$ of the pulse element should typically be $\beta \approx 55°$ for optimal 3Q recoupling [20]. $\tau_w$ represents a "window" during which the RF-field is turned off, and timed such that $N$ concatenated elements of duration $\tau_R = n\tau_r/N$ extend over exactly $n$ rotational periods $\tau_r = 2\pi/\omega_r$, where $\omega_r$ is the MAS frequency. As explained in [20,34], the performance of the $RN_n^v$ sequence is optimized when the fraction of the pulses relative the total duration of $\tau_R$ is minimized (and hence the fraction of the windows is maximized); this is specified by the *pulse fraction* $f_p$

$$f_p = \tau_R^{-1} \sum_{p=1}^{\text{pulses in } \mathcal{R}} \tau_p. \quad (2)$$

The $RN_n^v$ sequences as used here are constructed by a $N/2$-fold repetition of the sequence $\mathcal{R}_{\phi_R}\mathcal{R}_{-\phi_R}$, where $\phi_R = \pi v/N$ represents a phase-shift [21,32,33].

The corresponding 3Q phase-cycle $(\mathrm{R}N_n^v)3^1$, extending over the interval $T = 3n\tau_\mathrm{r}$, is formed from the sequence

$$(\mathrm{R}N_n^v)3^1 \equiv \left[\mathrm{R}N_n^v\right]_0\left[\mathrm{R}N_n^v\right]_{\frac{2\pi}{3}}\left[\mathrm{R}N_n^v\right]_{\frac{4\pi}{3}} \tag{3}$$

with the subscript denoting an overall phase-shift. The $(\mathrm{R}18_3^7)3^1$ scheme spans 9 rotational periods and may be formulated

$$(\mathrm{R}18_3^7)3^1 \equiv (\mathcal{R}_{70}\mathcal{R}_{-70})^9(\mathcal{R}_{190}\mathcal{R}_{50})^9(\mathcal{R}_{310}\mathcal{R}_{170})^9, \tag{4}$$

where the superscript $(\ldots)^9$ implies nine repetitions of the pulse sequence within parenthesis, with the subscripted phase-shift specified in degrees.

If $(\mathrm{R}18_3^7)3^1$ is applied to an ensemble of systems comprising at least three coupled spins at thermal equilibrium in a strong magnetic field, longitudinal polarization is converted into 3QC. This may be used in a triple-quantum filtration (3QF) experiment to select only spin triplets that may enter a 3QC spin ensemble state. Fig. 1A shows such an experimental pulse scheme, where it is assumed that the recoupled spin species $S$ (e.g., $^{13}$C) are surrounded by a network of abundant spins $I$ (e.g., $^1$H). The experiment starts by heteronuclear polarization transfer to the $S$ spins by cross-polarization from the $I$ spins, whereupon the latter is decoupled throughout the reminder of the experiment, for example using TPPM [35]. 3QC excitation is subsequently carried out by application of $q_\mathrm{exc}$ phase-shifted $\mathrm{R}18_3^7$ units of the $(\mathrm{R}18_3^7)3^1$ 3Q phase-cycle, giving the 3QC excitation interval $\tau_\mathrm{exc} = 3q_\mathrm{exc}\tau_\mathrm{r}$. The 3QC are converted back into observable 1QC by another $(\mathrm{R}18_3^7)3^1$ segment of duration $\tau_\mathrm{rec} = 3q_\mathrm{rec}\tau_\mathrm{r}$, followed by a $\pi/2$ read pulse and signal acquisition. Note that it is not necessary to use $q_\mathrm{exc} = q_\mathrm{rec}$ [31,36]. The reconversion block has an overall phase shift

$$\Phi_\mathrm{rec} = \Phi_\mathrm{rec}^0 + \Phi_\mathrm{3QF}, \tag{5}$$

where $\Phi_\mathrm{rec}^0$ is an odd integer multiple of $\pi/3$ (in our implementations equal to $\pi$) and $\Phi_\mathrm{3QF}$ is cycled in six steps to select solely the coherence transfer pathways $\pm 3 \rightarrow 0$ [37].

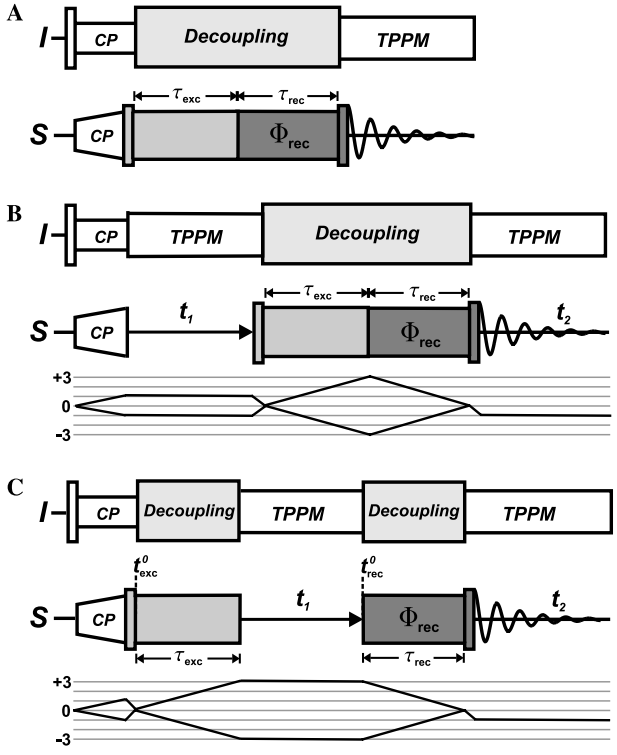


Fig. 1. Various pulse schemes incorporating triple-quantum filtration (3QF) using the 3Q recoupling sequence $(\mathrm{R}18_3^7)3^1$. (A) The prototype version, resulting in a 3QF $S$-spin spectrum; initially employing polarization transfer from abundant $I$-spins, followed by 3QC excitation with $(\mathrm{R}18_3^7)3^1$ (light shaded $S$ RF-channel blocks). The coherences are converted into longitudinal polarization by applying another sequence of $(\mathrm{R}18_3^7)3^1$ (dark shading), with a phase-shift $\Phi_\mathrm{rec}$ according to Eq. (5). (B) 3QF 1Q–1Q 2D correlation experiment. (C) 3Q–1Q 2D correlation experiment. All narrow rectangles represent $\pi/2$ pulses. The exploited coherence transfer pathway is indicated beneath each sequence (B and C).

### 2.2. 2D homonuclear correlation protocols

The 3QF experiment may be modified to build 2D homonuclear correlation schemes. Two such versions are shown in Figs. 1B and C.

In Fig. 1B, the evolution interval "$t_1$" is inserted prior to the 3QF stage, resulting in a 3QF 2D correlation experiment utilizing the 3Q recoupling sequence as a mixing period. First, each spin is evolving under its chemical shift during $t_1$. The single-quantum coherences are converted into $z$-polarization, which is subsequently filtered through 3QC, resulting in polarization transfer within triads of coupled spins. Hence, the resulting 2D spectrum reveals spin connectivities. This experiment is analogous to previously introduced approaches relying on a 2Q recoupling Hamiltonian [28,38], with the main distinction that the current 3QF version allows direct (as opposed to "relayed" [37], henceforth called "indirect" [31]) through-space polarization transfers between spins separated by *one as well as two bonds*. This is evidenced by the 3QF 1Q–1Q correlation $^{13}$C spectrum from a polycrystalline sample of [$^{13}$C$_3$]alanine (Fig. 2); cross-peaks appear between the C–C$^\alpha$ as well as C–C$^\beta$ pairs of spins. However, spin–spin correlations are only established provided that 3QC excitation is feasible. For instance, no 2D NMR peaks would appear from the same experiment performed on diluted [$^{13}$C$_2$]glycine, and this experiment may lead to spectral simplification in uniformly labeled macromolecules.

A pulse scheme for 3Q–1Q correlation spectroscopy is depicted in Fig. 1C: the evolution interval is now inserted *between* the pulse blocks for 3QC *excitation and reconversion*. This experimental strategy was previously introduced for $^1$H 3Q–1Q correlations [39] and was briefly discussed in the current context of second-order

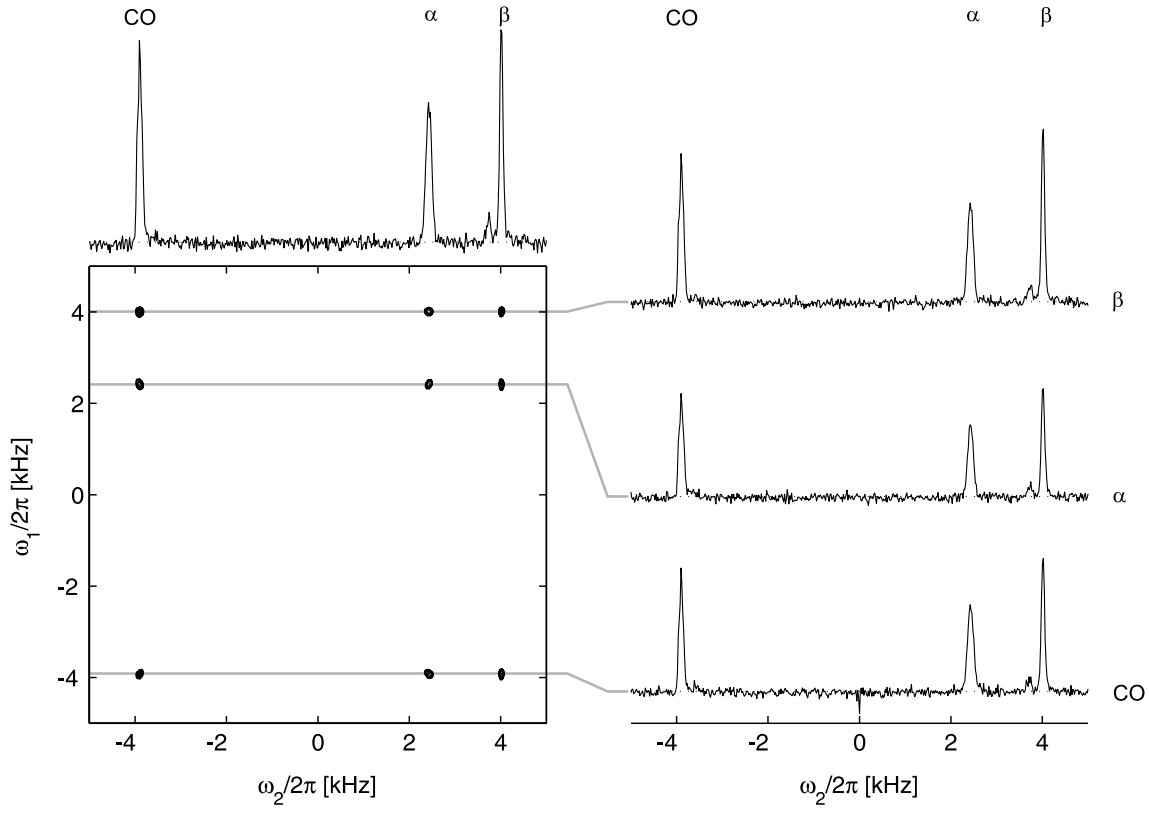


Fig. 2. 2D 3QF 1Q–1Q correlation spectrum from a powder of [U-$^{13}$C,$^{15}$N]L-alanine (partially deuterated), recorded at $B_0 = 4.7$ T and $\omega_r/2\pi = 7.6$ kHz, using the pulse scheme of Fig. 1B with equal durations of $(R18_3^7)3^1$ for 3QF excitation and reconversion: $\tau_{exc} = \tau_{rec} = 2.76$ ms (corresponding to $q_{exc} = q_{rec} = 7$). The recoupling pulses employed $\omega_{nut}^C/2\pi = 110$ kHz and $\mathcal{R}(\beta = 52°)$; $f_p = 0.33$. Proton decoupling nutation frequencies were $\omega_{nut}^H/2\pi = 110$ and 117 kHz during $^{13}$C pulses and windows of $(R18_3^7)3^1$, respectively, with $^1$H RF phases specified in [20].

based recoupling in [20]. During $t_1$, the triple-quantum coherences evolve under the sum of chemical shift interactions within the spin triad. Next, the 3QC are reconverted into observable transverse magnetization by another sequence of $(R18_3^7)3^1$ irradiation of duration $\tau_{rec}$ followed by a $\pi/2$ pulse and signal acquisition. The phase factor $\exp\{it_1(\omega_p^{iso} + \omega_q^{iso} + \omega_r^{iso})\}$ involving the sum of isotropic chemical shifts of the *pqr* spin triplet (anisotropic chemical shifts, producing sidebands in the $\omega_1$-dimension, are disregarded) is generally unique to each 3QC and corresponds to the $\omega_1$ coordinate in the 2D 3Q–1Q correlation spectrum. Fourier transformation of the $s(t_1,t_2)$ set produces a 2D spectrum that correlates each 3QC with its three corresponding single-quantum coherences. [$^{13}C_3$]alanine represents the simplest spin system producing only one peak in the $\omega_1$ dimension of its 3Q–1Q correlation spectrum (Fig. 3).

## 3. Second-order 3Q dipolar recoupling

This section briefly outlines the gist of generating a time-independent 3Q average Hamiltonian. A more detailed formulation may be found in [19,20].

### 3.1. Dipolar interaction under MAS

We consider a system of three spins-1/2 (of species *S*), denoted *p*, *q*, and *r* and coupled pair-wise as *pq*, *pr*, and *qr* by the through-space dipolar interaction. Other spin interactions such as chemical shifts and *J*-couplings are ignored. The Hamiltonian $H^\Lambda$ of a general spin interaction $\Lambda$ is a product of a component *m* of a *l*th rank spatial irreducible spherical tensor $A^\Lambda$, and a component $\mu$ of a $\lambda$th rank spin irreducible spherical tensor operator $T^\Lambda$ [22,23]. The spin and spatial parts are denoted $A_{lm}^\Lambda$ and $T_{\lambda\mu}^\Lambda$, respectively, with the components taking integer values in the range $-l \leqslant m \leqslant l$ and $-\lambda \leqslant \mu \leqslant \lambda$. The homonuclear *S*–*S* dipolar interaction is second rank with respect to rotations of its spatial and spin rank ($l = 2$ and $\lambda = 2$).

The high-field dipolar Hamiltonian for the coupling *pq* may be expressed

$$H_{pq}(t) = \omega_{pq}(t)\frac{1}{\sqrt{6}}\left\{2S_{pz}S_{qz} - \frac{1}{2}\left(S_p^+S_q^- + S_p^-S_q^+\right)\right\}, \quad (6)$$

where application of MAS imposes a time-dependence of the dipolar frequency according to

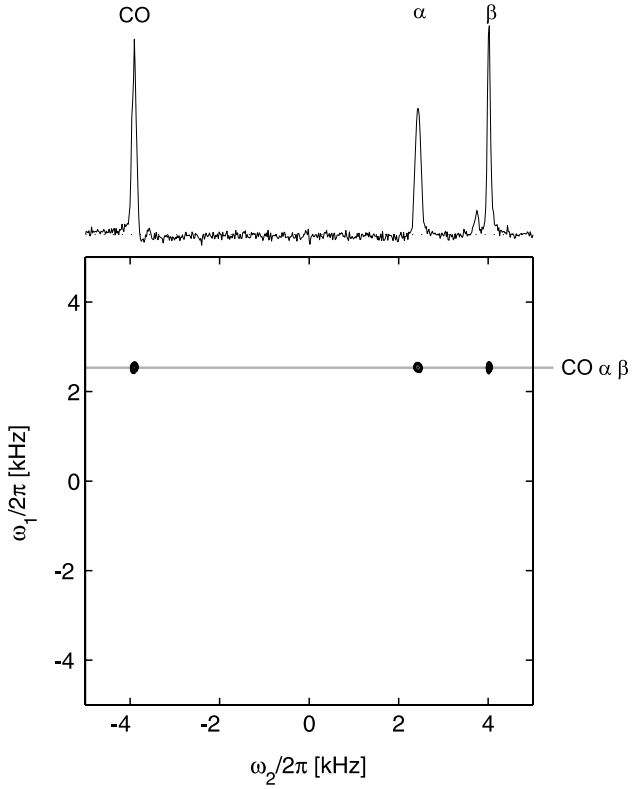


Fig. 3. 2D 3Q–1Q correlation spectrum of [U-$^{13}$C, $^{15}$N]L-alanine at 4.7 T with acquisition parameters as given in Fig. 2. The spectrum displays one peak in the $\omega_1$-dimension, at the 3QC frequency of the three $^{13}$C sites in the molecule.

$$\omega_{pq}(t) = \sum_{m=-2}^{2} [A_{2m}^{pq}]^R d_{m0}^2(\beta_{RL}) \exp\{-\mathrm{i}m(\alpha_{RL}^0 - \omega_r t)\}. \quad (7)$$

$d_{m0}^2(\beta)$ is a second-rank reduced Wigner element [40], and $\alpha_{RL}^0$ defines the rotor position at time origin $t = 0$. $[A_{2m}^{pq}]^R$ is the $m$th dipolar component in a *rotor frame* $R$ fixed on the sample holder; its $z$-axis subtends the angle $\beta_{RL} = \arctan\sqrt{2}$ with respect to the static magnetic field. The rotor-frame component is related to the coupling constant $b_{pq}$ by a sequence of rotations, involving an intermediate molecular frame $M$ that is fixed on an arbitrary fragment of the molecule

$$[A_{2m}^{pq}]^R = \sqrt{6} b_{pq} \exp\{-\mathrm{i}m\gamma_{MR}\} \sum_{m'=-2}^{2} D_{0m'}^2(\Omega_{PM}^{pq}) d_{m'm}^2(\beta_{MR}) \times \exp\{-\mathrm{i}m'\alpha_{MR}\} \quad (8)$$

with the dipolar coupling constant $b_{pq}$ related to the internuclear distance $r_{pq}$ and the gyromagnetic ratio $\gamma_S$, according to

$$b_{pq} = -\frac{\mu_0}{4\pi}\gamma_S^2 \hbar r_{pq}^{-3}. \quad (9)$$

The set of Euler angles $\Omega_{PM}^{pq}$ defines the orientation of the principal axis system $P$ (whose $z$-axis coincides with the $p$–$q$ internuclear vector). Likewise, the crystallite orientation relative to the rotor frame is parametrized by $\Omega_{MR}$, that are randomly distributed in a powder.

### 3.2. 3Q average Hamiltonian

In an RF field interaction representation, the dipolar Hamiltonian of spin-pair $pq$ may be expressed [41]

$$\tilde{H}_{pq}(t) = \sum_{\mu} \tilde{\omega}_{pq}(t) T_{2\mu}^{pq} \quad (10)$$

and the total Hamiltonian is given as a sum over the three pairs of dipolar couplings

$$\tilde{H}(t) = \sum_{IJ=pq,pr,qr} \sum_{\mu} \tilde{\omega}_{IJ}(t) T_{2\mu}^{IJ}. \quad (11)$$

A time-independent average Hamiltonian may be obtained by applying the Magnus expansion [42]

$$\overline{H} = \overline{H}^{(1)} + \overline{H}^{(2)} + \overline{H}^{(3)} + \cdots \quad (12)$$

over the period $T$ of a time-periodic pulse sequence starting at time-point $t^0$. This procedure leads to a series of time-independent average Hamiltonian expansion terms [22,23]:

$$\overline{H}^{(1)} = \frac{1}{T} \sum_{IJ=pq,pr,qr} \sum_{\mu} T_{2\mu}^{IJ} \int_{t^0}^{t^0+T} \mathrm{d}t\, \tilde{\omega}_{IJ}(t), \quad (13)$$

$$\overline{H}^{(2)} = (2\mathrm{i}T)^{-1} \sum_{\substack{IJ,KL=\{pq,pr,qr\} \\ IJ\neq KL}} \sum_{\mu_2,\mu_1} \left[T_{2\mu_2}^{IJ}, T_{2\mu_1}^{KL}\right] \times \int_{t^0}^{t^0+T} \mathrm{d}t' \int_{t^0}^{t'} \mathrm{d}t \tilde{\omega}_{IJ}(t') \tilde{\omega}_{KL}(t), \quad (14)$$

where the summation is over all distinct spin pairs, selected from the set of couplings $\{pq,pr,qr\}$. Note that we employ a perturbation order indexing starting at one, as in [43,44].

The aim in recoupling is traditionally to obtain the desired average Hamiltonian by means of Eq. (13): this is referred to as *first-order recoupling* and is effected by rotating the laboratory frame Hamiltonian by the sequence of RF pulses, such that the spin system is effectively evolving under a new, transformed Hamiltonian. However, we are interested in obtaining a 3Q average dipolar Hamiltonian, which is proportional to three-spin operators of the form $S_p^+ S_q^+ S_r^+$ and $S_p^- S_q^- S_r^-$. As the laboratory frame dipolar Hamiltonian may only be rotated into a linear combination of two-spin operators $T_{2\mu}$, three-spin 3Q operators are only achieved to second-order AHT: hence the terminology *second-order recoupling* [19,20,25]. According to Eq. (14), the ±3Q Hamiltonian terms arise from commutators involving a 1Q operator from one coupling pair (e.g., $T_{2\pm1}^{pq}$) and a 2Q operator ($T_{2\pm2}^{qr}$) from a *different* pair. In the presence of several interactions (chemical shifts and $J$-cou-

plings), the resulting first and second-order average Hamiltonians comprise a large number of contributions. The application of a $(\mathrm{R}N_n^v)3^1$ pulse sequence ensures that only 3Q and ZQ dipolar terms are recoupled [19,20]. The ZQ terms may be removed by another stage of supercycling, at a price of a slightly modified form of the 3Q average Hamiltonian [20]. Isotropic $J$-couplings also survive $(\mathrm{R}N_n^v)3^1$ schemes. While $J$-couplings commute with the 3Q Hamiltonian in three-spin systems, they interfere with the 3QC dynamics in larger systems. Illustrations of the impact from ZQ terms and $J$-couplings on the 3QC dynamics will be considered in Section 9; up to that point we ignore their effects.

The total second-order 3Q average Hamiltonian in a large spin system is a sum over the contributions from all distinct spin-triplets $pqr$, and may be expressed

$$\overline{H}_{3Q} = \sum_{p<q<r} \frac{1}{4}\left(\omega_{pqr} S_p^+ S_q^+ S_r^+ + \omega_{pqr}^* S_p^- S_q^- S_r^-\right). \tag{15}$$

The 3QC frequency $\omega_{pqr}$ is expressed as a sum over pairwise products of dipolar couplings $b_{pq}b_{pr}$, each multiplied by a scaling factor $\kappa$ depending on the particular recoupling sequence used. Its explicit expression is given in [20].

## 4. Definition of polarization transfer functions

In the following, we assume a system of $\mathcal{N}$ coupled spins-1/2, a single crystallite orientation parametrized by the Euler angles $\Omega_{MR}$ and that the intervals for excitation and reconversion of 3QC are equal: $\tau_{\mathrm{exc}} = \tau_{\mathrm{rec}} = \tau$. The function $f^{3Q}_{\rho_S \to \rho_T}$ describes the polarization transfer from a density operator of the *source* ensemble state $\rho_S \equiv \rho(t = t^0)$ going through 3QC to a *target* state $\rho_T$. In the superoperator formalism [37,45], it may be formulated

$$f^{3Q}_{\rho_S \to \rho_T}(\tau, \Omega_{MR}, \Phi^0_{\mathrm{rec}}) = \frac{\left(\rho_T \mid \widehat{U}^{\mathrm{rec}}(\tau, \Omega_{MR}, \Phi^0_{\mathrm{rec}})\widehat{P}^{(3)}\widehat{U}^{\mathrm{exc}}(\tau, \Omega_{MR}) \mid \rho_S\right)}{(\rho_S \mid \rho_S)} \tag{16}$$

with $\widehat{P}^{(3)}$ being a super-operator for filtering of 3QC. The propagation superoperator for 3QC excitation is

$$\widehat{U}^{\mathrm{exc}}(\tau, \Omega_{MR}) = \exp\{-\mathrm{i}\widehat{\overline{H}}^{\mathrm{comm}}_{3Q}\tau\}, \tag{17}$$

where the superscript 'comm' denotes a commutator superoperator: $\widehat{A}^{\mathrm{comm}}|B) \equiv |[A, B])$ [37,45]. The reconversion propagator is related to the corresponding excitation propagator through

$$\widehat{U}^{\mathrm{rec}}(\tau, \Omega_{MR}, \Phi^0_{\mathrm{rec}}) = \widehat{R}_z(\Phi^0_{\mathrm{rec}})\widehat{U}^{\mathrm{exc}}(\tau, \Omega_{MR})\widehat{R}_z(-\Phi^0_{\mathrm{rec}}), \tag{18}$$

where the $z$-rotation superoperator is given by $\widehat{R}_z(\Phi) = \exp\{-\mathrm{i}\Phi\widehat{S}_z^{\mathrm{comm}}\}$, and $\widehat{S}_z^{\mathrm{comm}}$ is the commutator superoperator for the total $z$-angular momentum operator $S_z = S_{pz} + S_{qz} + S_{rz} + \cdots$.

The transfer may take various 3QC pathways, as illustrated for the case of four coupled spins in Fig. 4.

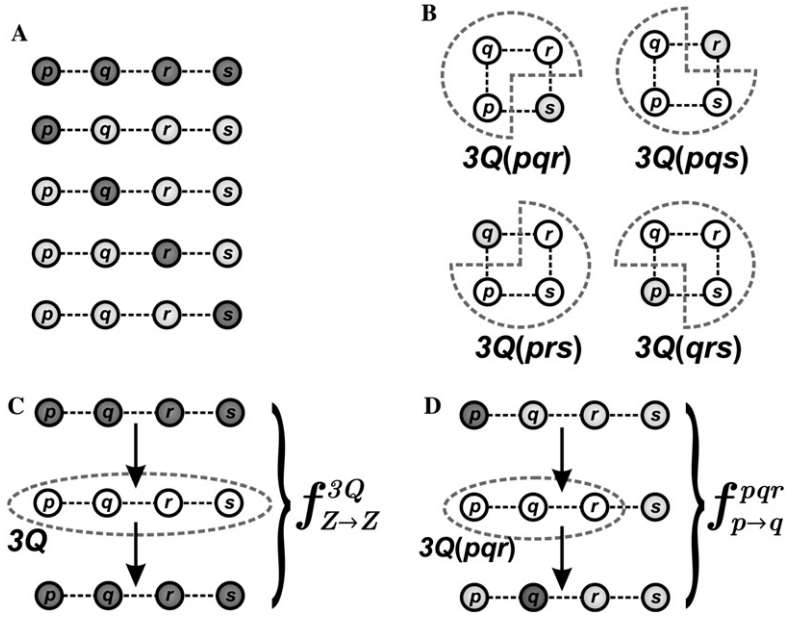


Fig. 4. (A) Depiction of systems comprising four coupled spins-1/2 ($p$, $q$, $r$, and $s$) in a linear configuration. Light and dark shadings indicate unpolarized and polarized spins, respectively. The system at the top has equal polarization of all spins, i.e., for an ensemble of such systems, the density operator is given by $\rho = S_z = S_{pz} + S_{qz} + S_{rz} + S_{sz}$. (B) Depiction of four distinct triple-quantum coherences. The spins involved in each 3QC are encircled, and the remaining spin is shaded. (C) Illustration of the transfer of total $z$-polarization ($\rho_S = S_z$) through total 3QC with the target state also corresponding to $z$-polarization ($\rho_T = S_z$): the 3QF amplitude as function of the 3QC excitation interval ($\tau$) is described by the function $f^{3Q}_{Z\to Z}(\tau)$. (D) Illustration of the transfer process $f^{pqr}_{p\to q}(\tau)$, implying that the initial polarization of spin $p$ is transferred through 3QC of spin triplet $pqr$ over to spin $q$.

We classify the various processes as follows: (i) transfer through total 3QC of the spin system, denoted by a superscript '3Q' ($f^{3Q}$) and (ii) transfer through *one* 3QC, in the following exemplified by 3Q($pqr$) and denoted $f^{pqr}$. If no superscript is specified for a transfer function, its result apply generally either to the total 3QC *or* one 3QC component.

In the cases considered here, both the source ($\rho_S$) and target ($\rho_T$) ensemble states correspond to $z$-polarization: we focus on transfer *either* from a system initially having *equal polarizations of all* spins, $\rho_S = S_z$, *or* with initial polarization of *only one* spin, say $\rho_S = S_{pz}$. Both scenarios are illustrated in Fig. 4A. We will employ the following shorthand transfer function notation: $f^{3Q}_{Z\to Z}$ denotes the transfer of total $z$-angular momentum through total 3QC coherence, $S_z \xrightarrow{3Q} S_z$, where '3Q' is given by the sum over all distinct spin-triplets (Fig. 4C). For example, in a three-spin system, 3Q = 3Q($pqr$), whereas in a four-spin system with spins ($p$,$q$,$r$,$s$), 3Q = 3Q($pqr$) + 3Q($pqs$) + 3Q($prs$) + 3Q($qrs$). The polarization transfer from spin $p$ to spin $q$ through 3Q($pqr$), $S_{pz} \xrightarrow{3Q(pqr)} S_{qz}$, is denoted $f^{pqr}_{p\to q}$ and shown in Fig. 4D. According to Eq. (16), these two examples correspond to

$$f^{3Q}_{Z\to Z}(\tau, \Omega_{MR}, \Phi^0_{\mathrm{rec}}) = \frac{(S_z|\widehat{U}^{\mathrm{rec}}(\tau, \Omega_{MR}, \Phi^0_{\mathrm{rec}})\widehat{P}^{(3)}_{\mathrm{tot}}\widehat{U}^{\mathrm{exc}}(\tau, \Omega_{MR})|S_z)}{(S_z|S_z)} \tag{19}$$

and

$$f^{pqr}_{p\to q}(\tau, \Omega_{MR}, \Phi^0_{\mathrm{rec}}) = \frac{(S_{qz}|\widehat{U}^{\mathrm{rec}}(\tau, \Omega_{MR}, \Phi^0_{\mathrm{rec}})\widehat{P}^{(3)}_{pqr}\widehat{U}^{\mathrm{exc}}(\tau, \Omega_{MR})|S_{pz})}{(S_{pz} \mid S_{pz})}, \tag{20}$$

respectively. The projection super-operator for filtering through the coherence 3Q($pqr$) is given by

$$\widehat{P}^{(3)}_{pqr} = \frac{|S^+_pS^+_qS^+_r)(S^+_pS^+_qS^+_r|}{(S^+_pS^+_qS^+_r|S^+_pS^+_qS^+_r)} + \frac{|S^-_pS^-_qS^-_r)(S^-_pS^-_qS^-_r|}{(S^-_pS^-_qS^-_r|S^-_pS^-_qS^-_r)} \tag{21}$$

and $\widehat{P}^{(3)}_{\mathrm{tot}}$ is the sum over all such 3QC projection operators:

$$\widehat{P}^{(3)}_{\mathrm{tot}} = \sum_{pqr}^{\text{all spin triplets}} \widehat{P}^{(3)}_{pqr}. \tag{22}$$

We condense the notation by observing that all polarization transfer functions depend on the reconversion phase as follows:

$$f_{\rho_S\to\rho_T}(\tau, \Omega_{MR}, \Phi^0_{\mathrm{rec}}) = f_{\rho_S\to\rho_T}(\tau, \Omega_{MR}, 0)\cos\{3\Phi^0_{\mathrm{rec}}\} \tag{23}$$

and assume that $\Phi^0_{\mathrm{rec}} = \pi$. However, this expression is only relevant for *one* given set of angles $\Omega_{MR} = \{\alpha_{MR}, \beta_{MR}, \gamma_{MR}\}$. We are also concerned with 3QC excitation dynamics in *powders*, necessitating the calculation of an orientational average over $\Omega_{MR}$

$$\left\langle f_{\rho_S\to\rho_T}(\tau, \Phi^0_{\mathrm{rec}} = \pi)\right\rangle_{\Omega_{MR}} = \frac{1}{8\pi^2}\int_0^{2\pi} \mathrm{d}\alpha_{MR}\int_0^{\pi} \sin\beta_{MR}\mathrm{d}\beta_{MR} \times \int_0^{2\pi} \mathrm{d}\gamma_{MR} f_{\rho_S\to\rho_T}(\tau, \Omega_{MR}, \pi). \tag{24}$$

In all that follows, we will report transfer functions abbreviated as:

$$f_{\rho_S\to\rho_T}(\tau) \equiv f_{\rho_S\to\rho_T}(\tau, \Omega_{MR}, \pi) \tag{25}$$

for single crystallite orientations, or the corresponding powder averages.

With our assumption that both source and target states involve longitudinal polarization, the 3QC transfer functions are real, and have the following properties, regardless of the size of the spin system:

(i) The *direction* of transfer is irrelevant up to a normalization factor involving the target state:

$$\frac{f_{\rho_S\to\rho_T}(\tau)}{(\rho_T|\rho_T)} = \frac{f_{\rho_T\to\rho_S}(\tau)}{(\rho_S|\rho_S)}. \tag{26}$$

This is well-known from magnetization-exchange experiments, where cross-peaks appearing symmetrically around the diagonal of the 2D spectrum have equal intensities, provided that the two exchanging spins are initially prepared with equal polarizations [37,46].

(ii) A function involving transfer to total $z$-polarization may be decomposed into a sum over transfers to each individual spin

$$f_{\rho_S\to Z}(\tau) = \sum_{p}^{\text{all spins}} f_{\rho_S\to p}(\tau). \tag{27}$$

(iii) Transfer through total 3QC is equal to the sum of transfer pathways through each distinct spin triplet

$$f^{3Q}_{\rho_S\to\rho_T}(\tau) = \sum_{pqr}^{\text{all triplets}} f^{pqr}_{\rho_S\to\rho_T}(\tau). \tag{28}$$

## 5. 3QC dynamics in three-spin systems

In this section, we discuss the analytical transfer functions obtained in a system comprising three coupled spins ($p$, $q$, and $r$). Upon 3QF, the initial $z$-polarization is distributed evenly over the spins: each contributes with 1/3 to the total transfer, leading to the expressions

$$f^{3Q}_{Z\to Z}(\tau) = 3f^{3Q}_{Z\to p}(\tau) = 3f^{3Q}_{p\to p}(\tau) = 3f^{3Q}_{p\to q}(\tau) = \frac{3}{4}\sin^2\left(\frac{1}{2}\omega_{\mathrm{eff}}\tau\right) \tag{29}$$

with the effective 3QC oscillation frequency $\omega_{\mathrm{eff}}$ given by

$$\omega_{\mathrm{eff}} = |\omega_{pqr}|. \tag{30}$$

These predictions are verified experimentally by the 2D spectrum acquired on [$^{13}C_3$]alanine (Fig. 2). It displays nine peaks, with very similar integrated intensities, as expected from Eq. (29). There are three diagonal peaks, whose integrals correspond to the values $f^{3Q}_{\alpha\to\alpha}, f^{3Q}_{\beta\to\beta}$, and $f^{3Q}_{CO\to CO}$ (evaluated for the excitation interval $\tau = 2.76$ ms). The remaining six signals are "cross peaks" originating from transfers between *distinct* spins; for example, the integrals of the peaks at the CO and $\alpha$ sites (the top slice of Fig. 2) represent the transfer functions $f^{3Q}_{\beta\to CO}$ and $f^{3Q}_{\beta\to\alpha}$, respectively.

Generally, a three-spin system subject to a 3Q Hamiltonian is oscillating between 3QC and ZQC, the latter transfer function represented by $f^{ZQ}_{Z\to Z}(\tau)$, and related to $f^{3Q}_{Z\to Z}(\tau)$ by the normalization condition $f^{ZQ}_{Z\to Z}(\tau)+f^{3Q}_{Z\to Z}(\tau) = 1$. 3QC excitation dynamics in a three-spin system using a 3Q average Hamiltonian is essentially identical to 2QC excitation in a two-spin system using a 2Q Hamiltonian of the form

$$\overline{H}_{2Q} = \frac{1}{2}\left(\omega_{pq}S^+_pS^+_q + \omega^*_{pq}S^-_pS^-_q\right). \tag{31}$$

Such 2Q average Hamiltonians are generated by recoupling sequences like C7 [41,43], DRAMA [47], MELODRAMA [38], and BABA [48], and leads to a 2QF function $f^{2Q}_{Z\to Z}(\tau)$ corresponding to

$$f^{2Q}_{Z\to Z}(\tau) = \sin^2(|\omega_{pq}|\tau). \tag{32}$$

The main differences between the two cases are that (i) the 3QC frequency $\omega_{pqr}$ is built from *products* of couplings ($\omega_{pqr}\sim b_{pq}b_{pr}$) and (ii) it is possible to effect loss-less $S_z\to S_z$ transfer through 2QC in a spin-pair from *one* crystallite orientation (Eq. (32)), whereas the optimum $S_z\to S_z$ transfer through 3QC in a spin triplet only amounts to 75% (Eq. (29)). This agrees with the theoretical upper unitary bound of polarization transfer [49]. However, reaching this in solid state NMR is only possible using the 3Q Hamiltonian of Eq. (15): alternative 3QC excitation techniques [50,51] provides less than 30% transfer efficiency for a single crystallite orientation.

The 3QF efficiency is lower in a powdered sample due to the orientational dependence of the recoupling. The maximum efficiency depends both on the spin system geometry and the particular 3Q recoupling sequence. For example, for $(R18^7_3)3^1$ it amounts to 51 and 56% for linear and equilateral spin triplet configurations, respectively. The latter geometry allows for 67% 3QF efficiency using another recoupling sequence $(R14^3_2)3^1$ (introduced in [20]). We believe this is the global maximum for 3Q recoupling in powders.

Fig. 5 shows a set of numerically simulated curves $f^{3Q}_{Z\to Z}(\tau)$ from $(R18^7_3)3^1$ using the pulse element $\mathcal{R}(\beta = 55°)$ at a spinning frequency $\omega_r/2\pi = 15.0$ kHz, and including only its 3Q average Hamiltonian part. They demonstrate that by passing total $z$-polarization

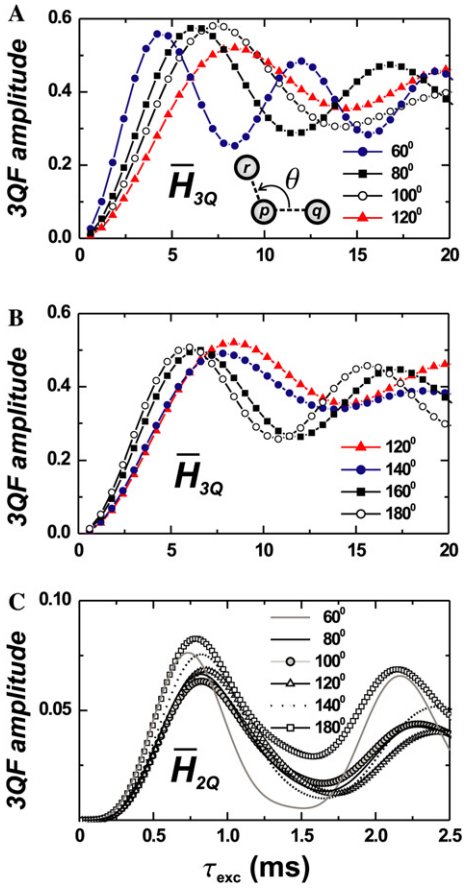


Fig. 5. (A and B) Numerical average Hamiltonian simulations [based on Eq. (19)] illustrating the dependence of the $f^{3Q}_{Z\to Z}(\tau)$ curves on the inter-bond angle $\theta$ (the intersecting angle between the $pq$ and $pr$ internuclear vectors) in a three-spin system, assuming the 3Q average Hamiltonian obtained from $(R18^7_3)3^1$ with element $\mathcal{R}(\beta = 55°)$ and pulse fraction $f_p = 0.30$ at a spinning frequency $\omega_r/2\pi = 15.0$ kHz. The dipolar couplings $b_{pq} = b_{pr} = -2250\cdot 2\pi$ rads$^{-1}$ were kept constant in all calculations, and the coupling $b_{qr}$ was adjusted according to values of $\theta$ in the range (a) $60°\leqslant\theta\leqslant 120°$ and (b) $120°\leqslant\theta\leqslant 180°$. (C) 3QF efficiency curves from the average Hamiltonian of the 2Q recoupling sequence POST-C7 [43], applied to an initial state of transverse polarization, $\rho_S = S_x$, to effect 3QC excitation at $\omega_r/2\pi = 5.2$ kHz.

through 3QC, it is feasible to estimate the inter-bond angle $\theta$ (defined as the angle between the $pq$ and $pr$ internuclear vectors). However, by comparing the transfer curves $f^{3Q}_{Z\to Z}(\tau,\theta)$ over the ranges $60°\leqslant\theta\leqslant 120°$ (Fig. 5A) and $120°\leqslant\theta\leqslant 180°$ (Fig. 5B) it is clear that a degeneracy occurs around $\theta\approx 130°$. The transfer function symmetry for relatively short excitation intervals obeys approximately the relationship $f^{3Q}_{Z\to Z}(\tau, 130°-\phi)\approx f^{3Q}_{Z\to Z}(\tau, 130°+\phi)$ for $0°\leqslant\phi\leqslant 50°$. This implies that an unambiguous determination of $\theta$ is only possible if the bond angle may first be assessed to be either smaller or larger than ≈130°. All values of $\theta$ give different oscillation frequencies over large values of $\tau$, but this is not of much help in practice for $^{13}C$ applications, as experiments need to the conducted over prohibitively long excitation intervals. In the range $\theta < 60°$, there

are strong variations in the 3QF curves: the 3QC build-up is much faster, as the dipolar coupling between the "non-bonded" nuclei exceeds those of the directly bonded ones ($b_{qr} > b_{pq} = b_{pr}$). However, those results are not presented as such spin topologies are rarely encountered.

As discussed in [17,50], an alternative route to 3QC excitation in three-spin systems is to apply a 2Q recoupling sequence to an initial state of transverse polarization. The 3QC dynamics by the two-spin 2Q dipolar Hamiltonian (Eq. (31)) may be evaluated analytically in three-spin systems [50]: Fig. 5C displays the resulting curves based on the average Hamiltonian of POST-C7 [43]. Apart from faster 3QC dynamics, as well as much lower 3QF amplitudes, the dependence of the dynamics on $\theta$ is markedly lower compared to the case of 3Q-recoupling. We conclude that the chances of geometry determinations in a three-spin system are higher using the 3Q recoupling sequence $(R18_3^7)3^1$ compared to using a 2Q recoupling sequence.

## 6. 3QC dynamics in four-spin systems

The possibilities of polarization transfers between the various members ($p$, $q$, $r$, and $s$) of a four-spin system are richer than that of three coupled spins. Some scenarios are depicted in Fig. 6. The corresponding transfer functions will be discussed in the following sections. Similarly to the three-spin case, all transfer functions involve an effective frequency

$$\omega_{\text{eff}} = (|\omega_{pqr}|^2 + |\omega_{pqs}|^2 + |\omega_{prs}|^2 + |\omega_{qrs}|^2)^{1/2}. \tag{33}$$

It is convenient to define the frequency

$$\Omega_p = (|\omega_{pqr}|^2 + |\omega_{pqs}|^2 + |\omega_{prs}|^2)^{1/2} \tag{34}$$

proportional to the root-mean-square over 3QC frequencies of *all triplets involving spin p*, as well as

$$\Omega_{pq} = (|\omega_{pqr}|^2 + |\omega_{pqs}|^2)^{1/2} \tag{35}$$

involving *both* spins *p and q*. The frequencies are related by $\Omega_p^2 = \Omega_{pq}^2 + |\omega_{prs}|^2$ and $\Omega_p^2 + |\omega_{qrs}|^2 = \omega_{\text{eff}}^2$. These definitions also apply to any permutation of the spin indices ($p$, $q$, $r$, and $s$), e.g., $\Omega_s^2 = |\omega_{pqs}|^2 + |\omega_{prs}|^2 + |\omega_{qrs}|^2$ and $\Omega_{qr}^2 = |\omega_{pqr}|^2 + |\omega_{qrs}|^2$, etc. The size of the transfer functions gives insight about the time-scale for which cross-peaks develop in a 2D correlation spectrum incorporating 3QF, as well as how their intensities relate to the coupling topology of the spin-system. The functions discussed here are proportional to powers of ratios involving individual 3QC frequencies relative to the effective 3QC frequency, e.g., $(|\omega_{pqr}|/\omega_{\text{eff}})^2$. As these ratios are always smaller than unity, the higher the power $n$, the smaller the magnitude of the ratio to the power of

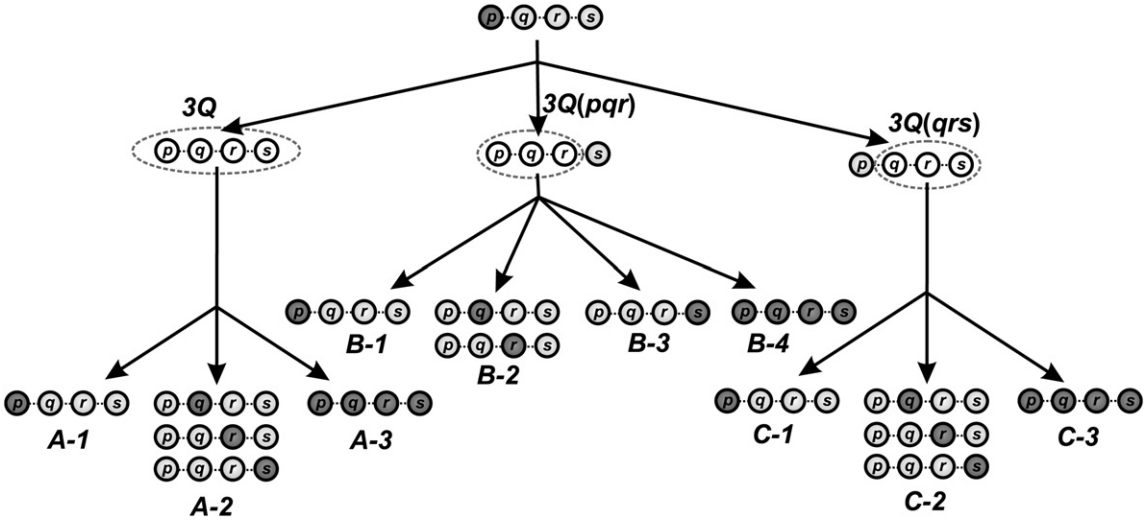


Fig. 6. Illustration of various polarization transfers from an ensemble of four coupled spins (labeled $p$, $q$, $r$, and $s$), starting with longitudinal polarization of spin $p$, i.e., $\rho_S = S_{pz}$. Three main 3QC pathways are indicated, where the left describes transfer through total triple-quantum coherence, resulting in the series of functions $f^{3Q}_{p\to\rho_T}(\tau)$. The polarization may be transferred either back to spin $p$ (case A-1), or to a distinct spin (A-2). In practice, the processes A-1 and A-2 are occurring simultaneously, and the sum over all possible pathways results in the process A-3, expressed by the function $f^{3Q}_{p\to Z}(\tau)$. The middle pathway corresponds to transfer through the 3QC of spins $pqr$ (associated with $f^{pqr}_{p\to\rho_T}(\tau)$), and may result either in transfer back to $p$ (case B-1), to spins $q$ and $r$ that are involved in 3Q($pqr$) (B-2), but also to spin $s$ *not* included in the coherence (B-3). The sum of these pathways corresponds to case B-4, represented by $f^{pqr}_{p\to Z}(\tau)$. The right part of the figure (C-1, C-2, and C-3) shows various scenarios for polarization transfer from a spin ($p$) *not* involved in the mediating 3QC. All depicted cases have experimental relevance: A-3, B-4, and C-3 occur generally in 3QF 1D experiments, whereas each of the pathways through 3Q($pqr$) and 3Q($qrs$) manifests as a peaks along the $\omega_1$-dimension in a 3Q–1Q experiment, with a corresponding peak along $\omega_2$ involving the frequency of the target spin. The transfers A-1, B-1, and C-1 give diagonal peaks in 3QF 1Q–1Q experiments, whereas those of A-2, B-2, B-3, and C-2 result in "cross-peaks."

$n$. Generally, a high power is accompanied with a high power of the trigonometric function that describes the cross-peak buildup (e.g., $\sin^n(\frac{1}{2}\omega_{\mathrm{eff}}\tau)$): the higher the power, the slower the cross-peak buildup.

### 6.1. Polarization transfers through total 3QC

The function associated with the transfer $S_z \xrightarrow{3Q} S_z$ for a single crystallite orientation is analogous to that of the three-spin case, except that the maximum transfer is reduced from 3/4 to 9/16

$$f^{3Q}_{Z\to Z}(\tau) = \frac{9}{16}\sin^2\left(\frac{1}{2}\omega_{\mathrm{eff}}\tau\right). \tag{36}$$

Starting from polarization of *one spin* and letting it pass through 3QC leads to an intensity distribution among the four spins in the 3QF spectrum (for a fixed value of $\tau$) according to (cf. case A-3 of Fig. 6)

$$f^{3Q}_{Z\to p}(\tau) = \frac{1}{4}f^{3Q}_{p\to Z}(\tau) = \frac{3}{16}\frac{\Omega_p^2}{\omega_{\mathrm{eff}}^2}\sin^2\left(\frac{1}{2}\omega_{\mathrm{eff}}\tau\right). \tag{37}$$

The relationship $f^{3Q}_{p\to Z}(\tau) = 4f^{3Q}_{Z\to p}(\tau)$ follows from Eq. (26) with the normalization $(S_z|S_z) = 4(S_{pz}|S_{pz})$. The factor $\Omega_p^2$, including the 3QC frequencies from all spin triplets involving $p$, appears as a weight factor of the amplitude of the transfer function. Hence, upon 3QF, the polarization distributes *unevenly* and the relative peak amplitudes in the 3QF spectrum carry information about the distributions of dipolar coupling strengths within the spin system.

Figs. 7A and B show a selection of numerically calculated transfer functions, all involving total $z$-polarization ($S_z$) as source state for a single crystallite orientation (A) and a powder (B) in the case of a linear spin configuration. As expected, the maximum value of the function $f^{3Q}_{Z\to Z}(\tau)$ is 0.5625 from a single crystallite, whereas the powder average maximum amounts only to 0.38. This spin topology emphasizes the dipolar effects of nearest neighboring spins, since maximal attenuation is effected for couplings between more distant spins through the $r^{-3}$ dependence. A high relative 3QF

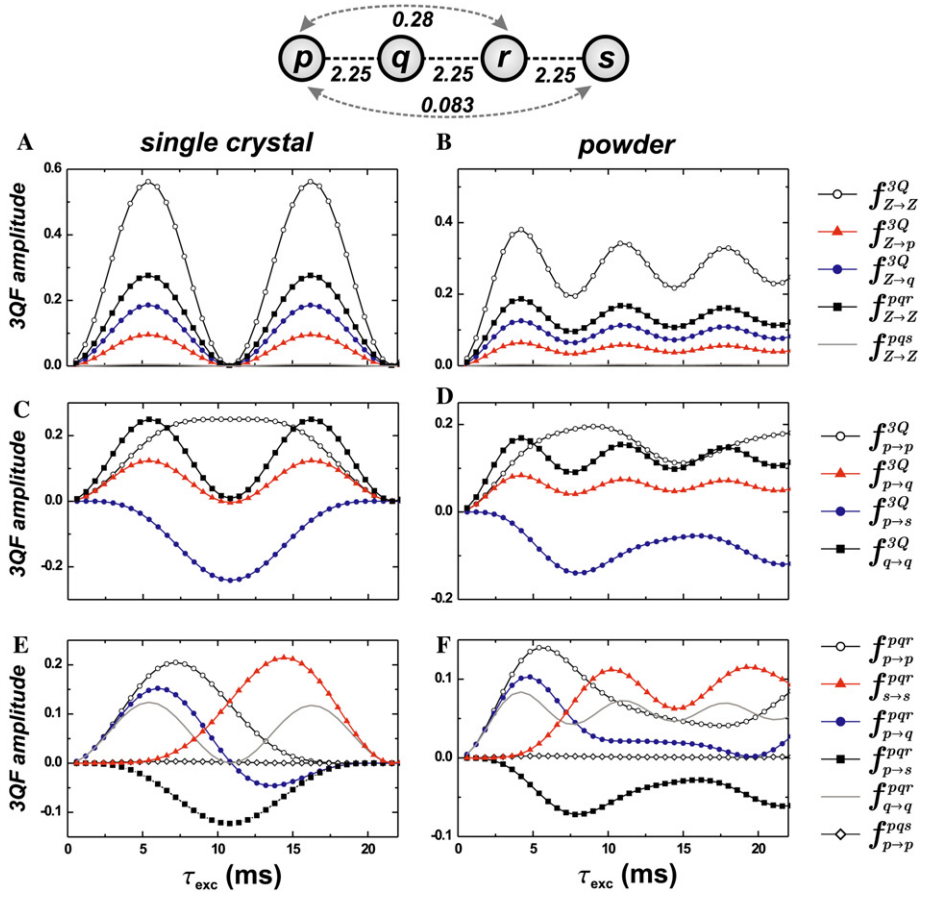


Fig. 7. Numerical average Hamiltonian simulations of using $(\mathrm{R18}_3^7)3^1$ [$\mathcal{R}(\beta = 55°), f_p = 0.30$] at $\omega_r/2\pi = 15.0$ kHz on a system of four coupled $^{13}$C, arranged in a linear configuration with equal internuclear distances ($r = 1.5$ Å) between nearest neighbors. Note that all dipolar vectors coincide. The corresponding magnitudes of the dipolar coupling constants are given in kHz as indicated at the top of the figure. The left panel (A, C, and E) displays simulations for a single crystallite orientation $\{\alpha_{PR}, \beta_{PR}, \gamma_{PR}\} = \{0, 40°, 0\}$, whereas the right panel (B, D, and E) represents powder averages. (A and B) Transfer functions involving total $z$-polarization as either source or target ensemble states (or both). (C and D) Transfers from one spin to another through total 3QC. (E and F) Transfers between spins through the 3QC of *one* spin triplet, 3Q($pqr$). Note that all plots have equal horizontal but different vertical scales.

amplitude of a given spin results from large dipolar couplings to its neighbors. These results are representative also for other four-spin chains. For the present set of dipolar couplings (Fig. 7), we obtain relative peak amplitudes from spins $p{:}q{:}r{:}s$ according to 0.170:0.330:0.330:0.170, i.e., a quartet with the intensities of the two "inner" spins ($q$, $r$) of the chain being almost exactly twice as large as those from the terminal ones ($p$, $s$). Other coupling topologies provide different peak intensity patterns in the 3QF spectrum. For example, if the $q$–$r$ and $r$–$s$ distances are set 1.5 and 1.25 times longer, respectively, than that between $p$–$q$, the amplitude distribution changes into 0.268:0.330:0.325:0.076.

On the other hand, assume that we start with polarization of spin $p$, and consider the transfer $S_{pz} \xrightarrow{3Q} S_{pz}$, i.e., spin $p$ is *both* the *source and target*, as depicted by case A-1 in Fig. 6. The corresponding function $f^{3Q}_{p\to p}(\tau)$ evaluates as

$$f^{3Q}_{p\to p}(\tau) = \frac{\Omega_p^2 F_p^2}{\omega_{\text{eff}}^4}\sin^2\left(\frac{1}{4}\omega_{\text{eff}}\tau\right) = \frac{\Omega_p^2}{\omega_{\text{eff}}^4}\left\{|\omega_{qrs}|^2 + \Omega_p^2\cos^2\left(\frac{1}{4}\omega_{\text{eff}}\tau\right)\right\}\sin^2\left(\frac{1}{4}\omega_{\text{eff}}\tau\right), \tag{38}$$

where $F_p^2$ is a sum of two terms; one proportional to $\Omega_p^2$, dependent on all dipolar couplings involving spin $p$, and $|\omega_{qrs}|^2$ which involves *all* couplings *but those to p*

$$F_p = \left\{|\omega_{qrs}|^2 + \Omega_p^2\cos^2\left(\frac{1}{4}\omega_{\text{eff}}\tau\right)\right\}^{1/2}. \tag{39}$$

Note that for short excitation intervals ($\frac{1}{4}\omega_{\text{eff}}\tau \ll 1$), $F_p^2 \approx |\omega_{\text{eff}}|^2$ and the initial buildup for $f^{3Q}_{p\to p}$ is proportional to $\Omega_p^2\tau^2/16$.

The transfer through total 3QC to a *distinct* target spin $q$ (case A-2 of Fig. 6) corresponds to

$$f^{3Q}_{p\to q}(\tau) = \frac{1}{4}\frac{\Omega_{pq}^2}{\omega_{\text{eff}}^2}\sin^2\left(\frac{1}{2}\omega_{\text{eff}}\tau\right) - \frac{|\omega_{prs}|^2|\omega_{qrs}|^2}{\omega_{\text{eff}}^4}\sin^4\left(\frac{1}{4}\omega_{\text{eff}}\tau\right). \tag{40}$$

This function is a sum of two opposing terms. The first is proportional to $\Omega_{pq}^2/\omega_{\text{eff}}^2$; it dominates at short 3QC excitation intervals and leads to a positive transfer amplitude in a 3QF 3Q–1Q correlation experiment. The second term is negative and proportional to the product of frequencies $-|\omega_{prs}|^2|\omega_{qrs}|^2/\omega_{\text{eff}}^4$; it is characterized by a significantly slower transfer, although this term may dominate for large values of $\tau$.

Some representative curves are shown in Figs. 7C and D: they are relevant in 3QF 1Q–1Q 2D correlation experiments as they describe polarization transfers between various spins within the system. For the present dipolar coupling network, we get the following set of transfer processes: $f^{3Q}_{p\to p} = f^{3Q}_{s\to s}$; $f^{3Q}_{q\to q} = f^{3Q}_{r\to r}$; $f^{3Q}_{p\to q} = f^{3Q}_{r\to s} = f^{3Q}_{p\to r} = f^{3Q}_{q\to s}$ as well as the two "unique" and distinct cases $f^{3Q}_{q\to r}$ and $f^{3Q}_{p\to s}$. The function $f^{3Q}_{q\to r}$ is not displayed, as it has an almost identical buildup to $f^{3Q}_{q\to q}$. It is evident from the simulations that the fastest transfer occurs for $f^{3Q}_{q\to q}$, being roughly twice as that of $f^{3Q}_{p\to q}$ and $f^{3Q}_{p\to p}$, whereas $f^{3Q}_{p\to s}$ provides a significantly slower buildup and with a negative amplitude.

### 6.2. Polarization transfers between individual spins through one 3QC

We now turn our attention to inter-spin polarization transfer processes through each *individual* triple-quantum coherence of the system; they are relevant for predicting the distribution of amplitudes in slices along the 1Q dimension in 2D 3Q–1Q correlation experiments. Although this class of transfers will be exemplified with 3Q($pqr$), analogous expressions are obtained upon permutations of the spin labels. All these functions are proportional to the frequency $|\omega_{pqr}|^2$ and the trigonometric function $\sin^2(\frac{1}{4}\omega_{\text{eff}}\tau)$. We first consider transfers where both source and target spins are part of the mediating 3QC, as illustrated by case B-2 of Fig. 6. The generic transfer function may be expressed

$$f^{pqr}_{p\to q}(\tau) = \frac{|\omega_{pqr}|^2 F_p^2 F_q^2}{\omega_{\text{eff}}^6}\sin^2\left(\frac{1}{4}\omega_{\text{eff}}\tau\right), \tag{41}$$

where the functions $F_p^2$ and $F_q^2$ (Eq. (39)) depends on the source and target spins, respectively. The special case when the source and target spins are equal then corresponds to B-1 of Fig. 6 and the transfer function casts as

$$f^{pqr}_{p\to p}(\tau) = \frac{|\omega_{pqr}|^2 F_p^4}{\omega_{\text{eff}}^6}\sin^2\left(\frac{1}{4}\omega_{\text{eff}}\tau\right) = \frac{|\omega_{pqr}|^2}{\omega_{\text{eff}}^6}\left\{|\omega_{qrs}|^2 + \Omega_p^2\cos\left(\frac{1}{4}\omega_{\text{eff}}\tau\right)\right\}^2\sin^2\left(\frac{1}{4}\omega_{\text{eff}}\tau\right). \tag{42}$$

Note that, as the functions $F_p^2$ and $F_q^2$ tend to $\omega_{\text{eff}}^2$ in the limit of short excitation intervals $\tau$, the initial slopes of the functions $f^{pqr}_{p\to p}(\tau)$ and $f^{pqr}_{p\to q}(\tau)$ are generally equal and proportional to $|\omega_{pqr}|^2\tau^2/16$, as illustrated by the numerical simulations in Figs. 7E and F.

In all cases considered so far, both source and target spins were involved in the mediating 3QC. Transfers are, however, possible where either the source or target spins are *not* part of the mediating coherence. Examples include $S_{pz} \xrightarrow{3Q(pqr)} S_{sz}$ and $S_{sz} \xrightarrow{3Q(pqr)} S_{qz}$. These indirect transfers are slow and occur over longer mixing periods in correlation experiments. The transfer from *one* spin, subsequently *involved in the* 3QC, to a target spin *not* involved in that coherence, is illustrated by case B-3 of Fig. 6 and associated with the function

$$f^{pqr}_{p\to s}(\tau) = -2\frac{|\omega_{pqr}|^2 F_p^2 \Omega_s^2}{\omega_{\text{eff}}^6}\sin^2\left(\frac{1}{8}\omega_{\text{eff}}\tau\right)\sin^2\left(\frac{1}{4}\omega_{\text{eff}}\tau\right). \tag{43}$$

Note the *negative sign*, indicating that the resulting NMR peak amplitude of the transfer from spin $p$ to spin $s$ is negative. From the symmetries of the transfer functions, an analogous expression is obtained for the transfer from a source spin not involved in the 3QC to a spin being part of the mediating 3QC, e.g., the functions $f^{pqr}_{s\to p}(\tau)$ and $f^{qrs}_{p\to s}(\tau)$. The latter case is illustrated by C-2 of Fig. 6 and also simulated in Figs. 7E and F.

In a four-spin system, there is only one case where *neither* the *source nor target* spins are part in the mediating 3QC, namely if they are equal as in the case $S_{pz} \overset{3Q(qrs)}{\longrightarrow} S_{pz}$ (C-1). The resulting transfer function is given by

$$f^{qrs}_{p\to p}(\tau) = 4\frac{|\omega_{qrs}|^2\Omega_p^4}{\omega_{\mathrm{eff}}^6}\sin^4\left(\frac{1}{8}\omega_{\mathrm{eff}}\tau\right)\sin^2\left(\frac{1}{4}\omega_{\mathrm{eff}}\tau\right). \qquad (44)$$

Note that despite the amplitude of the function is positive like the "direct" transfers of Eq. (41), it is a very slow process due to the factor $\sin^4(\frac{1}{8}\omega_{\mathrm{eff}}\tau)$. Hence, such cross-peaks develop even slower than those associated with the indirect processes $f^{pqr}_{p\to s}(\tau)$ and $f^{qrs}_{p\to q}(\tau)$ (Eq. (43)). This is confirmed by the simulations in Fig. 7.

### 6.3. Polarization transfer of $S_z$ through one 3QC

Using the relationships between polarization transfers and individual spins through 3Q($pqr$), we can calculate the functions involving $S_z$ as source or target. The transfer from any of the spins contributing to the 3QC [e.g., 3Q($pqr$)] is obtained from Eq. (27)

$$f^{pqr}_{p\to Z}(\tau) = f^{pqr}_{p\to p}(\tau) + f^{pqr}_{p\to q}(\tau) + f^{pqr}_{p\to r}(\tau) + f^{pqr}_{p\to s}(\tau) \qquad (45)$$

giving the expression

$$f^{pqr}_{Z\to p}(\tau) = \frac{1}{4}f^{pqr}_{p\to Z}(\tau) = \frac{3}{8}\frac{|\omega_{pqr}|^2F_p^2}{\omega_{\mathrm{eff}}^4}\sin\left(\frac{1}{4}\omega_{\mathrm{eff}}\tau\right)\sin\left(\frac{1}{2}\omega_{\mathrm{eff}}\tau\right). \qquad (46)$$

This process corresponds to B-4 of Fig. 6. In the case of transfer of total polarization through a given 3QC (e.g., 3Q($pqr$)) to the target spin *not involved in that spin triplet*, the process $S_z \overset{3Q(pqr)}{\longrightarrow} S_z$ is represented by

$$f^{pqr}_{Z\to s}(\tau) = \frac{1}{4}f^{pqr}_{s\to Z}(\tau) = -\frac{3}{4}\frac{|\omega_{pqr}|^2\Omega_s^2}{\omega_{\mathrm{eff}}^4}\sin^2\left(\frac{1}{8}\omega_{\mathrm{eff}}\tau\right) \times \sin\left(\frac{1}{4}\omega_{\mathrm{eff}}\tau\right)\sin\left(\frac{1}{2}\omega_{\mathrm{eff}}\tau\right). \qquad (47)$$

Finally, the transfer of total polarization through *one* 3QC, $S_z \overset{3Q(pqr)}{\longrightarrow} S_z$, corresponds to

$$f^{pqr}_{Z\to Z}(\tau) = \frac{9}{16}\frac{|\omega_{pqr}|^2}{\omega_{\mathrm{eff}}^2}\sin^2\left(\frac{1}{2}\omega_{\mathrm{eff}}\tau\right) \qquad (48)$$

from which Eq. (36) follows by summing over the four distinct triple-quantum coherences as in Eq. (28). Eq. (48) predicts that the transfer involving each pathway is weighted by the ratio between the square of its 3QC frequency and the effective frequency. From the set of dipolar couplings in Fig. 7, we obtain two large and equal ratios $|\omega_{pqr}|^2/\omega_{\mathrm{eff}}^2 \approx 0.491$ associated with the two 3QC involving solely directly connected nuclei, i.e., 3Q($pqr$) and 3Q($qrs$), and two small ratios for 3Q($pqs$) and 3Q($prs$): $|\omega_{pqs}|^2/\omega_{\mathrm{eff}}^2 \approx 0.0087$. This implies that the total transfer is exclusively occurring through the 3QC of spin triplets $pqr$ and $qrs$, as corroborated by the simulations of Fig. 7A, where the grey line corresponding to the function $f^{pqs}_{Z\to Z}$ is hardly discernible.

## 7. 3QC dynamics in larger clusters

The dependence of the 3QC buildup on the dimensionality and size of the spin system is compared further in Fig. 8. The powder averaged transfers $f^{3Q}_{Z\to Z}$ were simulated for linear chains comprising three, four, and six spins, as well as from four and six spins arranged at the vertices of a tetrahedron and octahedron, respectively. The symmetric three-dimensional spin networks provide significantly faster 3QC excitation than any of the linear chains. For the chains, the initial rate of 3QC excitation enhances as the number of participating spins increase, while the maximum attainable 3QF amplitude is largest for the three-spin system. The excitation intervals providing optimal 3QF *amplitude* in each case are: 9.7 ms (three-spin chain), 6.8 ms (four-spin chain), 4.0 ms (tetrahedron), and 2.5 ms (octahedron).

The most interesting feature of these *powder* averaged transfer function simulations is the optimal efficiency achieved in the tetrahedral and octahedral case: the value 0.532 of the former is *only marginally lower than the theoretical efficiency from a single crystal*

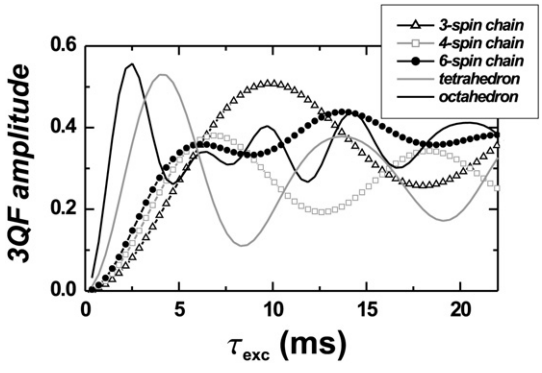


Fig. 8. Comparison of powder averaged transfer functions $f^{3Q}_{Z\to Z}(\tau)$ for linear chains of three, four, and six spins, as well as spins at the vertices of tetrahedra and octahedra, in all cases assuming coupling constants of −2251 Hz between nearest neighbors. Other simulation parameters are as in Fig. 7. Note the enhanced 3QC buildup rate as either the number of spins or the dimensionality of the spin topology increases.

(0.5625). This is to the best of our knowledge the first demonstration in MAS NMR of essentially identical MQF efficiencies obtained from a powder and single crystal. The recoupling sequence $(\mathrm{R}14_3^2)3^1$ [20] provided the even higher value $f_{Z\to Z}^{3Q}(\tau_{\mathrm{opti}}) = 0.553$ (simulations not shown). No attempts have been made to verify this experimentally, but these predicted values from powders are unprecedented for high-order MQC excitation under MAS conditions in systems comprising more than three spins.

## 8. High-order multiple-quantum excitation

In large spin systems, MQC orders higher that three will develop under the action of a 3Q Hamiltonian. The selection rules for the particular coherence orders created depend on the nature of the average dipolar Hamiltonian, the size of the spin system as well as on the initial density operator. Selection rules have previously been thoroughly discussed for a variety of average Hamiltonians [11], in particular for those comprising two-spin 1Q [4,52] and 2Q operators [5–8]. In this section, we discuss the action of a three-spin 3Q Hamiltonian when applied to a density operator corresponding to either longitudinal ($\rho(0) = S_z$) or transverse ($\rho(0) = S_x$) polarization. These results were obtained through the commutator properties of $\rho(0)$ and $\overline{H}_{3Q}$.

### 8.1. Longitudinal polarization

Assuming an ensemble of infinitely large spin systems, initially prepared with longitudinal polarization of each spin, the three-spin 3Q Hamiltonian effects multiple-quantum excitation by changing the coherence order by $\pm 3$. Therefore, all coherence orders being integer multiples of three ($M = \pm 3, \pm 6, \pm 9$) will develop successively. However, in finite spin clusters, the MQC excitation under a given Hamiltonian is more selective, and also depends on the size of the system $\mathcal{N}$. For example, it has been shown that it is *not* possible to excite 4QC in four-spin systems using a two-spin 2Q Hamiltonian [4,7,8,11]. Similarly, if $\mathcal{N}$ is an *even* multiple of three (i.e., $\mathcal{N} = 3k$ with $k$ even), then the extreme coherence orders $M = \pm\mathcal{N}$ are not excitable by $\overline{H}_{3Q}$. This implies that from an ensemble of six-spin systems at thermal equilibrium, only ZQC and 3QC may be excited. This is verified by the numerical simulation in Fig. 9A, where the powder averaged transfer functions $f_{Z\to Z}^{MQ}(\tau)$ are plotted for all MQC orders *generated* by $(\mathrm{R}18_3^7)3^1$. Because the MQ dynamics is confined to ZQC and 3QC, the 3QC excitation is almost as efficient as in three-spin systems (compare the simulations in Figs. 5 and 9). However, 6QC develop in larger systems, as shown by the seven-spin simulation of Fig. 9B.

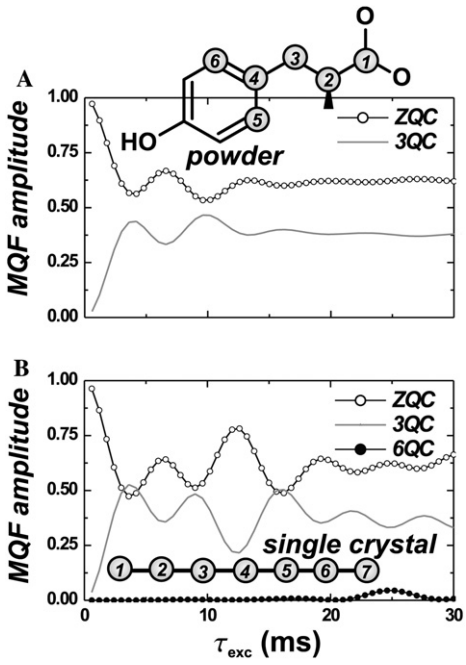


Fig. 9. Development of multiple-quantum coherences when applying the average Hamiltonian generated by $(\mathrm{R}18_3^7)3^1$ at $\omega_r/2\pi = 15.0$ kHz to spin systems prepared with equal *longitudinal* spin polarizations ($\rho(0) = S_z$). The curves correspond to MQF functions $f_{Z\to Z}^{MQ}(\tau)$ for the following cases: (A) a powder of six-spin fragments of tyrosine and (B) a single linear chain of seven $^{13}$C spins, oriented as $\{\alpha_{PR}, \beta_{PR}, \gamma_{PR}\} = \{0, 45°, 0\}$ with equal internuclear distance ($r = 1.5$ Å) between nearest neighbors. All dipolar couplings were considered. Only the curves for *excited* coherences are shown, implying that only ZQC and 3QC develop from the six-spin ensemble.

### 8.2. Transverse polarization

We continue the discussion assuming the spin system ensemble is initially prepared with 1QC (transverse polarization). The excitation dynamics is generally more complicated than the previous case with longitudinal polarization. We first note that 4QC cannot directly be excited from 1QC (e.g., $[S_s^+, S_p^+ S_q^+ S_r^+] = 0$). In general, $\pm$1QC are instead first converted into $\mp$2QC (regardless of the size of the spin system) which develop on a time-scale linear in the excitation interval $\tau$. In three and four spin systems, the ensemble state is therefore oscillating between 1QC and 2QC, analogously to the partition between ZQC and 3QC in the case of longitudinal polarization.

The smallest spin system which may excite coherence orders higher than two is that of five spins, for which both 4QC and 5QC are generated. The 5QC excitation may be rationalized through the schematic process

$$S_p^+ \overset{S_p^- S_q^- S_r^-}{\longrightarrow} S_{pz} S_q^- S_r^- \overset{S_p^- S_s^- S_t^-}{\longrightarrow} S_p^- S_q^- S_r^- S_s^- S_t^- \tag{49}$$

which implies that 5QC are created on a time-scale $\sim\tau^2$. 4QC generally develop slower than 5QC, as the former may only arise through "three-step" processes, according to

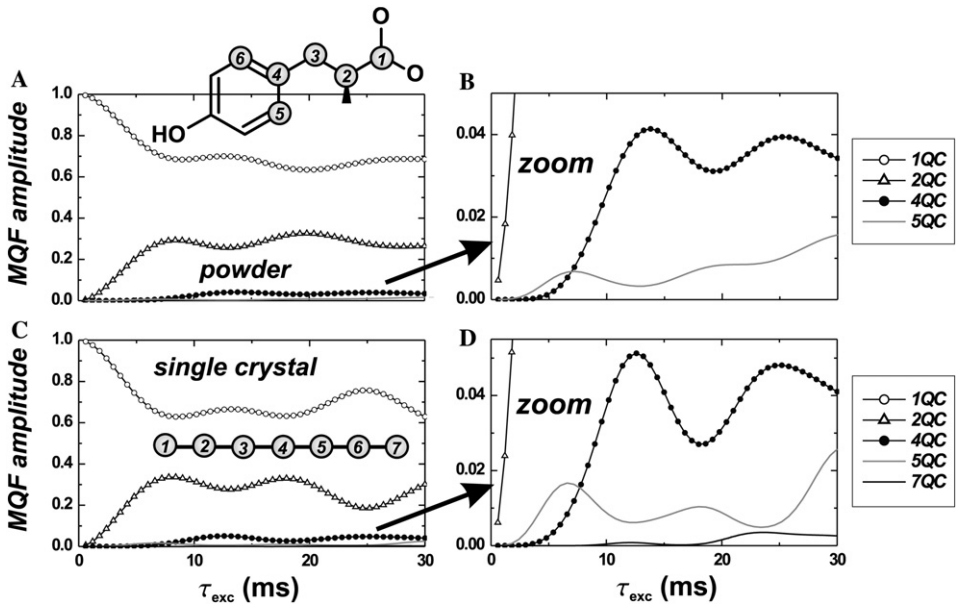


Fig. 10. Simulations as in Fig. 9, but instead starting from transverse polarization: $\rho(0) = S_x$. Diagrams B and D correspond to zoomed regions of A and C, respectively, and reveal the rather weak excitation of the extreme coherence-order.

$$S_p^+ \overset{S_p^- S_q^- S_r^-}{\rightarrow} S_{pz} S_q^- S_r^- \overset{S_r^+ S_s^+ S_t^+}{\rightarrow} S_{pz} S_q^- S_{rz} S_s^+ S_t^+ \overset{S_p^+ S_q^+ S_r^+}{\rightarrow} S_p^+ S_{qz} S_r^+ S_s^+ S_t^+ . \quad (50)$$

Hence, the +1Q operator of spin $p$ is converted into a five-spin operator $S_p^+ S_{qz} S_r^+ S_s^+ S_t^+$, corresponding to +4QC of the quartet *prst*. Altogether, this implies a cubic dependence on the excitation interval ($\sim\tau^3$) for 4QC excitation.

From an ensemble state of transverse polarization, the trilinear 3Q Hamiltonian creates in general all coherence orders $M \leqslant \mathcal{N}$, *except* those being integral multiples of three. This is illustrated by the simulations involving six and seven spins, shown in Figs. 10A and C, respectively. In the former case, 2QC, 4QC, and 5QC are excited from 1QC, whereas for the latter, weak 7QC excitation also occurs. Despite that 5QC grows on a time-scale $\sim\tau^2$, whereas 4QC only develop as $\tau^3$, the *amount* of 4QC will dominate that of 5QC over longer excitation intervals (see Figs. 10B and D), as there are a larger number of possible routes to create 4QC compared to 5QC.

## 9. 2D correlation schemes: experiments and simulations

In Section 2 we demonstrated the 1Q–1Q and 3Q–1Q correlation techniques for the three-spin system of [$^{13}C_3$]alanine. Here we discuss them further in the context of the nine coupled $^{13}C$ of [U-$^{13}C$]tyrosine.

### 9.1. 1Q–1Q correlation spectrum

The tyrosine 1Q–1Q correlation spectrum is shown in Fig. 11, together with slices at the isotropic chemical shifts of each site (right panel) as well as the 3QF 1Q spectrum, obtained by projecting the 2D spectrum onto the $\omega_2$ axis. For the latter, the total signal intensity is mainly concentrated among the aromatic $^{13}C$. As in the 2D spectrum from alanine (Fig. 2), off-diagonal cross-peaks arise between all sites separated by one or two bonds. For example, consider the slice at the chemical shift of the chemically equivalent $\delta,\delta'$ sites: in addition to the diagonal peak from the transfer $f^{3Q}_{\delta,\delta'\rightarrow\delta,\delta'}$, strong off-diagonal peaks appear due to transfers from $\delta,\delta'$ to the directly bonded $\varepsilon,\varepsilon'$ and $\gamma$-sites, as well as two weaker signals to the $\zeta$ and $\beta$ sites separated by two bonds. For the excitation interval employed ($\tau_{exc} = 1.58$ ms), several slices also manifest weak signals originating from polarizations transmitted over three bonds: for instance, there is transfer from the $\zeta$-site to the $\gamma$-site, as well as between the $\beta$ and $\varepsilon,\varepsilon'$ sites.

We simulated some transfer functions using AHT. Two examples are shown in Fig. 12, corresponding to the transfers from sites $\alpha$ (A,B) and $\zeta$ (C,D) to their surrounding $^{13}C$. The left diagrams of each row (A,C) result from including only the 3Q terms of the second-order average Hamiltonian, as in all previously presented calculations. However, the $(R18^7_3)3^1$ sequence leaves the (first-order) homonuclear $J$-couplings intact and also recouples a set of ZQ dipolar terms ($\overline{H}^{(2)}_{ZQ}$). These Hamiltonian terms were included in the simulations of Figs. 12B and D, which reveal significantly perturbed 3QC dynamics, even at short excitation intervals (<1 ms), relative to that in Figs. 12A and C. Additional simulations (not shown) indicate that 3QC dephasing induced by the ZQ average Hamiltonian terms is the main reason for the alterations of the 3QC oscillations and the severe polarization transfer losses, as discussed further

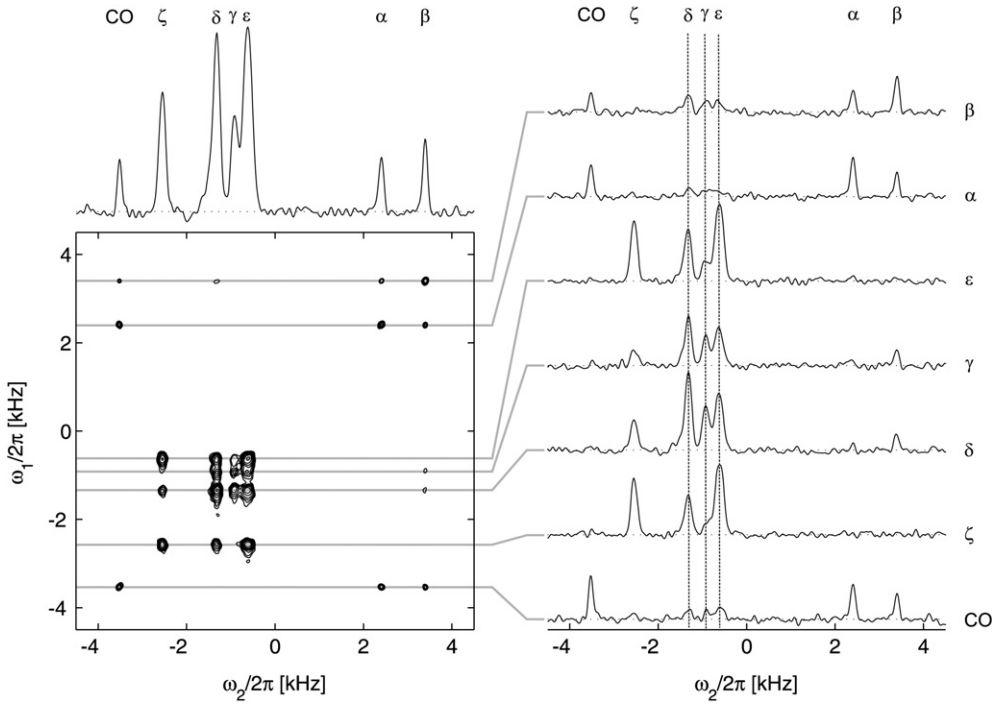


Fig. 11. 2D 3QF 1Q–1Q correlation spectrum from a powder of [U- $^{13}C$,$^{15}N$]L-tyrosine, recorded using the pulse scheme in Fig. 1B with $(R18_3^7)3^1$ for 3QF [$\mathcal{R}(\beta = 53°)$; $f_p = 0.33$]. The right stack of spectra comprises slices taken at the isotropic chemical shift position of each site. The experiment employed similar parameters as in the case of alanine (caption of Fig. 2), except $\tau_{exc} = \tau_{rec} = 1.58$ ms ($q_{exc} = q_{rec} = 4$).

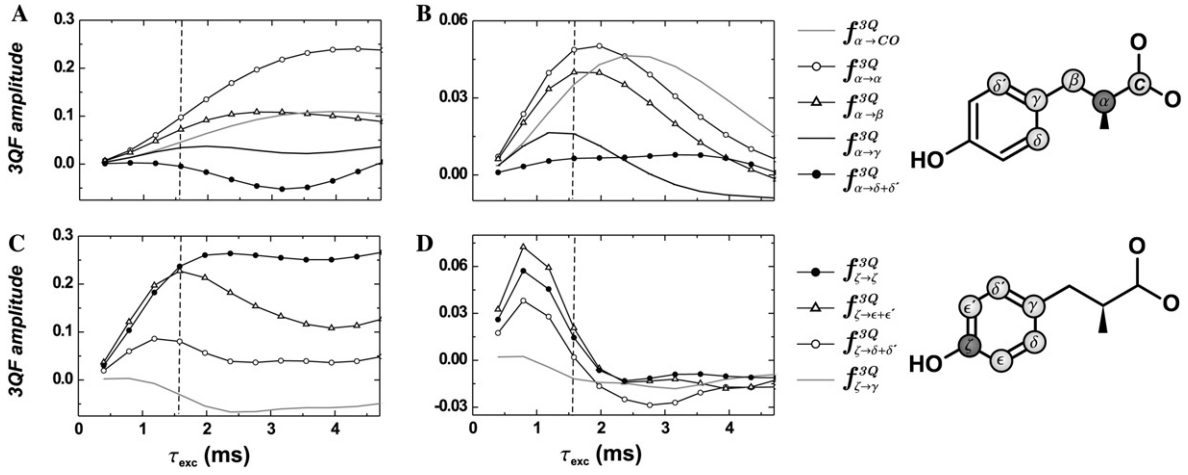


Fig. 12. Simulated polarization transfers when applying $(R18_3^7)3^1$ to a six-spin fragment of the tyrosine molecule, assuming initial polarization only of the α-site (A and B) and ζ-site (C and D). The AHT simulations employed the experimental parameters of Fig. 11 but included only couplings among the marked spins. Chemical shifts were not taken into account: ideally they are suppressed to second-order AHT. The dashed lines indicate the excitation interval used experimentally in Fig. 11. The simulations in (A and C) were based on only the 3Q part $(\overline{H}_{3Q}^{(2)})$ of the second-order average Hamiltonian, whereas diagrams (B and D) resulted after also including the ZQ contributions $(\overline{H}_{ZQ}^{(2)})$ and *J*-couplings $(H_J^{(1)})$.

in [20]. The *J*-couplings in the absence of ZQ terms do not affect the 3QC oscillations significantly over time-scales up to ~3 ms, but reduces the transfer amplitudes by ~25%.

Apart from differences in the amplitudes of the curves in Fig. 12, there are no major *qualitative* discrepancies at the excitation interval $\tau_{exc} = 1.58$ ms employed experimentally (indicated by dashed lines in Fig. 12), except that the three-bond transfer $f_{\alpha\to\delta,\delta'}^{3Q}$ is negative for the calculations incorporating 3Q terms only, whereas those also including ZQ dipolar and *J*-coupling terms have positive amplitudes. The latter case agrees qualitatively with the experimental result of Fig. 11, which displays a weak positive peak at the δ resonance. However, both simulated polarization transfers $f_{\zeta\to\gamma}^{3Q}$ of Figs. 12C and D predict negative values throughout the range of $\tau_{exc}$,

whereas the corresponding experimental peak is positive. Similar differences are found between experiments and simulations for the 3Q–1Q correlation experiment presented below. RF inhomogeneity is attributed as the main reason for these deviations.

The discrepancies between experimental and calculated results are reasons for concern. They preclude extraction of structural information (dipolar couplings and bond angles) from our current experiments combined with AHT calculations, whereas numerically exact simulations are not feasible with our computer resources for the spin system size required to faithfully simulate tyrosine. Unfortunately, confining the calculations of six-spin fragments of the nine coupled $^{13}$C could potentially introduce systematic errors in the calculated transfer functions. Additionally, there are several other *experimental* obstacles complicating a quantitative analysis. First, the assumption of equal spin polarizations at the start of the recoupling interval is in general not valid due to different cross-polarization efficiencies for distinct $^{13}$C sites, leading to unequal cross-peak intensities ($f_{p\to q}(\tau) \neq f_{q\to p}(\tau)$) in the correlation experiments [46]. This must be accounted for by a careful analysis, as must differences in relaxation of the spins during excitation and reconversion of 3QC, in turn related to the major experimental obstacle, namely to isolate the recoupled $^{13}$C spins from surrounding protons. $^{13}$C–$^{1}$H couplings perturb the 3QC dynamics and leads in particular to severe signal losses [20].

### 9.2. 3Q–1Q correlation spectrum

Fig. 13 shows the 3Q–1Q correlation spectrum of tyrosine, together with slices taken through each of the seven distinct triple-quantum coherences. This correlation spectrum provides enhanced resolution along the $\omega_1$ dimension and easier assessment of spin–spin connectivities than the 1Q–1Q experiment. The amplitude of each peak appearing in the slice of 3Q($pqr$) represents the value of the function $f^{pqr}_{Z\to j}$, where strong signals are only expected if spin $j$ belongs to the spin triplet $pqr$. Five of the seven triple-quantum coherences comprise three chemically inequivalent nuclei with distinct isotropic chemical shifts, manifested by three resolved peaks at the respective chemical shift frequency in the $\omega_2$ dimension. However, the two triplets $\gamma\delta\delta'$ and $\zeta\varepsilon\varepsilon'$ involve two chemically equivalent nuclei, hence displaying only two peaks in the 3QF slice.

Fig. 14 presents numerically simulated transfer functions for three distinct 3QC. By comparing the left and right diagrams of each row, it may be concluded that the simulations incorporating ZQ-terms and $J$-couplings result in ~50% loss for each transfer process. The two triple-quantum coherences 3Q($\alpha\beta\gamma$) and 3Q($\delta\varepsilon\zeta$) involve three *distinct* spins. The simulations displayed in Figs. 14A–D predict an evenly distributed polarization among the three spins in the 3QF spectrum. This is in reasonable agreement with the integrated experimental amplitudes of Fig. 13. However, the *total integrated* experimental intensity over the 3Q($\alpha\beta\gamma$)-slice relates to

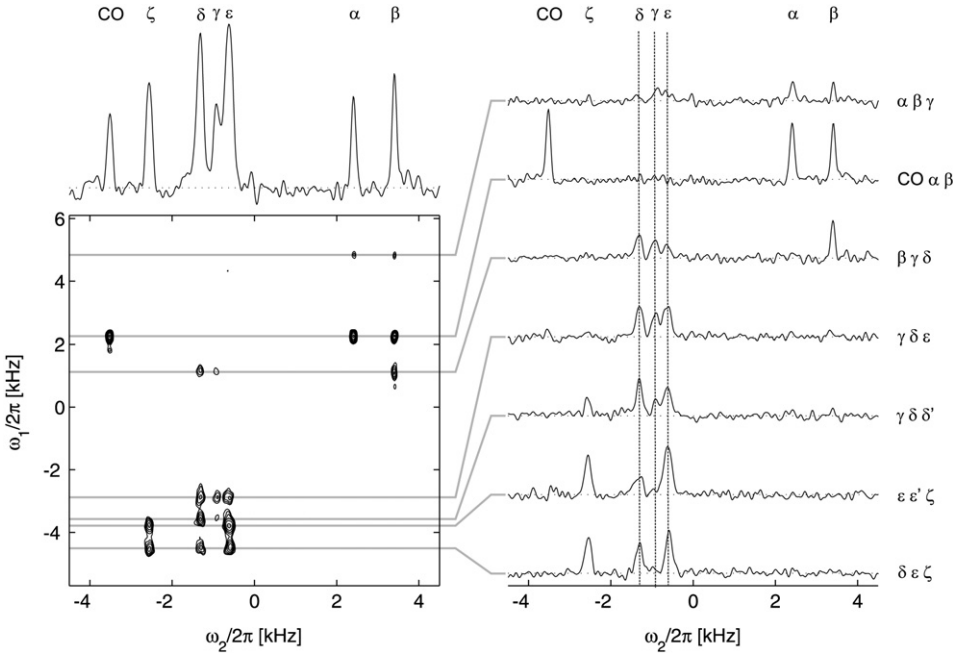


Fig. 13. 2D 3Q–1Q correlation spectrum acquired on [U-$^{13}$C, $^{15}$N]L-tyrosine with the pulse scheme of Fig. 1C and similar acquisition parameters to those of Figs. 2 and 11, except that $\omega_r/2\pi = 7.2$ kHz and *distinct* excitation and reconversion intervals were employed: $\tau_{exc} = 1.67$ ms ($q_{exc} = 4$) and $\tau_{rec} = 0.83$ ms ($q_{rec} = 2$). The experimental conditions corresponded to using $(R18^7_3)3^1$ with $\mathcal{R}(55°)$ and $f_p = 0.31$. The stack of 1D spectra represents slices at each of the seven 3QC frequencies present in $\omega_1$.

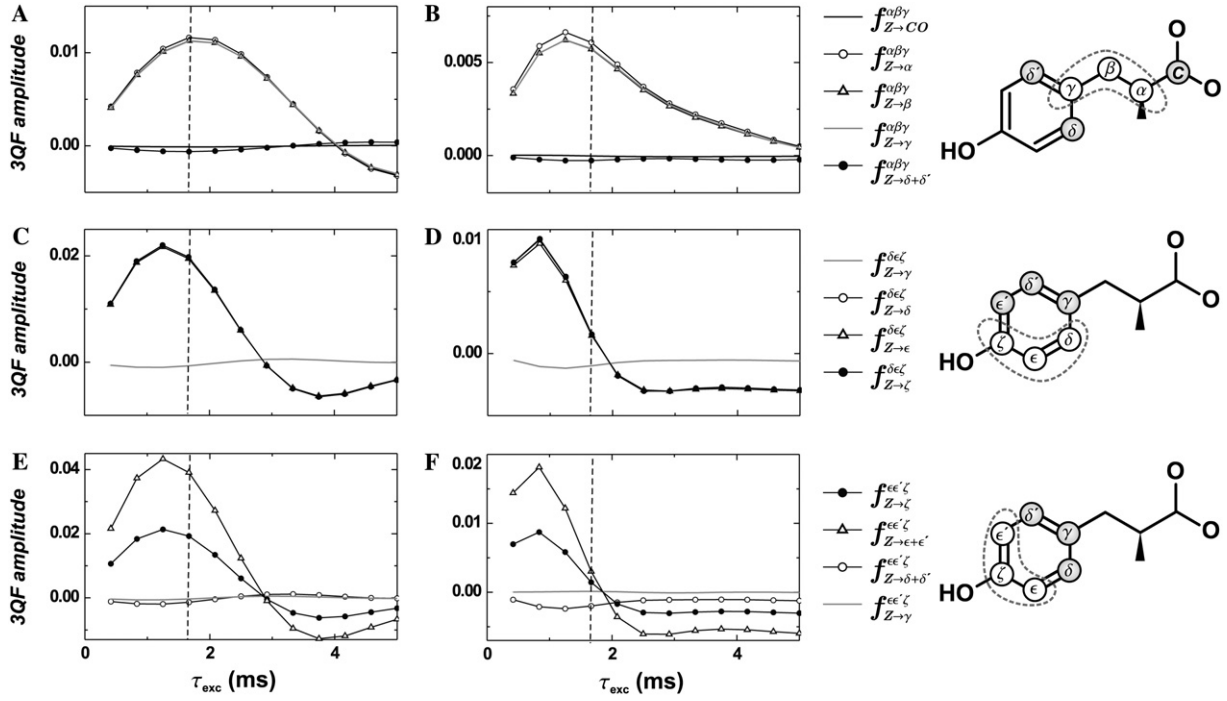


Fig. 14. Simulated transfers of total $z$-polarization through the following 3QC: (A and B) 3Q($\alpha\beta\gamma$); (C and D) 3Q($\delta\varepsilon\zeta$); and (E and F) 3Q($\varepsilon\varepsilon'\zeta$) for three different six-spin fragments of the tyrosine molecule. The AHT simulations employed experimental parameters of Fig. 13 and couplings among the marked spins (right part of figure). The simulations in (A, C, and E) assumed only the 3Q part of the second-order average Hamiltonian, whereas those in (B, D, and F) resulted after also including the ZQ and $J$-coupling contributions. Calculations were mimicking the acquisition protocol of [31,36], incorporating an incremented excitation interval, while keeping the reconversion interval fixed at $\tau_{rec} = 0.83$ ms. The dashed lines mark the value $\tau_{exc} = 1.67$ ms used in Fig. 13.

that of 3Q($\delta\varepsilon\zeta$) as 1:4.4, which agrees with neither of the simulations, regardless if ZQ and $J$-coupling contributions are included or not.

Figs. 14E and F display the transfer functions involving 3Q($\varepsilon\,\varepsilon'\zeta$). Although the simulated curves in F are significantly damped relative those of E, both AHT calculation predict that $f^{\varepsilon\varepsilon'\zeta}_{Z\to\varepsilon,\varepsilon'} = 2.0 \cdot f^{\varepsilon\varepsilon'\zeta}_{Z\to\zeta}$, i.e., that the spectral amplitude at the $\varepsilon$,$\varepsilon'$ chemical shift is twice that of the $\zeta$-site. This is in good agreement with the ratio of the integrated experimental amplitudes of the $\zeta$ and $\varepsilon$,$\varepsilon'$ peaks, estimated as 1.0:1.8.

## 10. Experimental and numerical methods

The experimental protocols (Fig. 1) were implemented on powders of 99% [U-$^{13}$C,$^{15}$N]L-alanine and [U-$^{13}$C,$^{15}$N]L-tyrosine at 4.7 T on a Varian/Chemagnetics Infinity spectrometer. The alanine sample was isotopically $^{2}$H-labeled at the $C^{\alpha}$(≈90%) and $C^{\beta}$(≈25%) positions. The samples were restricted to the center 1/3 of 4 mm rotors to reduce RF inhomogeneity. All experiments employed $^{13}$C nutation frequencies of ≈50 and 110 kHz during cross-polarization and pulses of the $(R18^7_3)3^1$ sequence, respectively. During signal acquisition, high-power proton decoupling ($\omega^H_{nut}/2\pi \approx 90$ kHz) was effected by CW-decoupling for alanine and TPPM [35] for tyrosine. CW was applied during the evolution interval $t_1$ for both samples. With recycle delays of 5 s (alanine) and 10 s (tyrosine), a 2D acquisition took typically 15 and 30 h for alanine and tyrosine, respectively. Specific acquisition parameters are given for alanine in the caption of Fig. 2, and for tyrosine in Figs. 11 and 13. A major experimental obstacle is to effect reasonably efficient heteronuclear $^{1}$H–$^{13}$C decoupling; this is well-known to be problematic when simultaneously applying $^{13}$C recoupling pulses [29,31,41,53,54]. Additional information about proton decoupling during application of 3Q-recoupling sequences is given in [20].

We employed the TPPI scheme [37] to obtain purely absorptive 2D spectra with sign discrimination along both spectral dimensions. For the 3QF 1Q–1Q experiments, the phase of the cross-polarization pulse was incremented for every consecutive $t_1$-value ($t_1 = \mathrm{m}\Delta t_1$) according to $\Phi^{1Q}_{TPPI} = \frac{\pi}{2}\mathrm{m}$ whereas for the 3Q–1Q correlations the phase shift $\Phi^{3Q}_{TPPI} = \frac{\pi}{6}\mathrm{m}$ was added both to the cross-polarization and 3QC excitation blocks. As explained in detail in Appendix A, a $t_1$-dependent phase shift of $m\Delta t_1\omega_r/3$ should be added to the phase $\Phi_{3QF}$ in Eq. (5) to allow an unrestricted spectral width in $\omega_1$, i.e., an arbitrary $t_1$-incrementation when using the recoupling sequence $(R18^7_3)3^1$.

The analytical transfer functions were obtained using *Mathematica* [55]. All numerical simulations started by

constructing the second-order 3Q Hamiltonian of Eq. (15), numerically diagonalizing it, and calculating the relevant transfer function according to Eq. (16). We verified the equivalence between the analytical results from *Mathematica* and the numerically calculated curves. AHT is strictly only valid at completed cycles of $(\mathrm{R18}_3^7)3^1$, i.e., when $\tau_{\mathrm{exc}}$ incremented in steps of $9\tau_{\mathrm{r}}$. This was used in all numerical calculations, except for those of Figs. 12 and 14, which employed sampling at completed $\mathrm{R18}_3^7$ sequences. All simulations, except parts of Figs. 5, 9, and 10, represent powder averages, typically calculated over 538 ZCW orientations [56–58]. The simulations of tyrosine assumed dipolar couplings and Euler transformation angles calculated from the atomic coordinates of [59].

## 11. Concluding remarks

In this article, we explored MQC excitation by a three-spin 3Q dipolar Hamiltonian in poly-crystalline powders comprising clusters of coupled spins-1/2 under MAS conditions. These results are complementary to previous investigations of MQC dynamics governed by 1Q and 2Q effective Hamiltonians [4–6,8,9,12].

We presented analytical expressions predicting the buildup of total 3QC as function of excitation interval in three and four-spin systems (initially prepared with longitudinal polarization), as well as the distribution of intensities among the individual spins in the 3QF NMR spectrum. The buildup of 3QC in a three-spin system was shown numerically to be dependent on the molecular geometry, and should in ideal cases allow for determining the intersection angle between two internuclear vectors. However, we have not verified this experimentally. A spin triplet subject to a three-spin 3Q Hamiltonian evolves similarly to a spin-pair under a two-spin 2Q Hamiltonian. The 3Q recoupling dynamics in a four-spin system share many features with a three-spin system subject to a 2Q Hamiltonian: this may be verified by comparing the analytical 3QF expressions of Section 6 with those in [50].

The most prominent feature of 3Q recoupling is the highly efficient 3QC filtration delivered from powders: the upper theoretical limit in three-spin systems amounts to ~67%. This number is only slightly lower than the maximal efficiency for 2QF in spin-pairs using a 2Q recoupling sequence (~73%). Interestingly, spin configurations also offering unusually high 3QF efficiencies are tetrahedral and octahedral clusters, for which the *powder* averaged 3QF efficiency may exceed ~55%, which is only marginally lower than the theoretical values from a *single* crystal. The optimal 3QF efficiency depends to some extent on the spin system size ($\mathcal{N}$) and its geometry, and also on the orientational dependence of the 3Q Hamiltonian terms of the pulse sequence employed, but 35–55% 3QF efficiency may ideally be expected in moderately large spin clusters. These numbers are several times higher than the theoretical efficiencies of previous methods for 3QC excitation in rotating solids [50,51].

In ensembles of larger spin clusters, higher-order MQC develop by the action of a 3Q Hamiltonian. We considered two cases where all spins are prepared with equal longitudinal or transverse polarizations. In the former case, all coherence orders $M$ being integral multiples of 3 are excited, except for the extreme orders $M = \pm\mathcal{N}$ if the cluster-size is an *even* multiple of three. Similar restrictions apply for an ensemble of four-spin clusters initially prepared with transverse magnetization: 4QC is not excited, and the spin system ensemble is oscillating between 1QC and 2QC. On the other hand, if a 3Q recoupling sequence is applied to systems involving more than four spins and prepared with transverse polarization, all multiple-quantum orders will develop (except for $M = 0, \pm 3, \pm 6, \ldots$).

We also demonstrated two 2D NMR protocols involving 3Q recoupling. They correlate either 1QC or 3QC, respectively, during $t_1$ with 1QC during acquisition ($t_2$). The 1Q–1Q 2D spectrum contains cross-peaks manifesting correlations between coupled spins separated by one or two bonds, whereas the 3Q–1Q protocol separates the various 3QC from each spin triplet in the sample. While experimental demonstrations on [U-$^{13}$C]L-alanine and L-tyrosine qualitatively established all expected correlations from these two known structures, the experiments could *not* be *quantitatively* reproduced by the AHT simulations, and hence no structural information is to be expected *directly* from the current second-order 3Q recoupling sequences discussed in this paper. An advantage with these 3Q correlation experiments compared to similar experiments involving 2QC, is indeed the "three-body" character of the trilinear 3Q average Hamiltonian: *potentially* geometric information may be obtained about a spin triad through 3Q recoupling.

There are two distinct problems involved in our current experimental protocols, which need consideration in future developments: (i) Heteronuclear decoupling during application of 3Q recoupling sequences is currently insufficient, leading to signal losses and potentially erroneous 2D spectral amplitudes. (ii) The second problem is more fundamental in that the 3Q phase-cycles discussed here do *not* provide a *pure* 3Q average Hamiltonian, but also recouple second-order ZQ dipolar terms. As discussed in [20], the ZQ terms may be removed by another stage of supercycling, thereby re-establishing all theoretical predictions of this work, which assumed "pure 3Q recoupling." However, the supercycles are no longer $\gamma$-encoded [60], limiting the 3Q–1Q correlation experiment in that the $t_1$-incrementation must be in steps of the rotational period $\tau_{\mathrm{r}}$ to avoid spectral artefacts.

In summary, we have demonstrated that polarization transfer through 3QC is a promising candidate for obtaining geometric information (such as inter-bond angles), but due to shortcomings of the currently available 3Q recoupling pulse sequences, they cannot directly provide this information by experimentally recording 3QF amplitudes as function of the excitation interval. Yet the sequences deliver higher 3QF efficiencies than previous schemes, and should nevertheless be useful as 3QC generators in any 3QC-based experiment. We believe that one of the most useful applications for the 3Q recoupling approach lies in experiments for measuring multiple peptide torsion angles in [$^{13}C_3$]alanine residues by combining the 2D 3Q–1Q correlation experiment with the technique described in [17].

## Acknowledgments

This work was supported by the Swedish Research Council (VR) and the Lars Hiertas Minne Foundation. We thank Zheng Weng for instrumental help and Dick Sandström for providing the alanine sample.

## Appendix A. Second-order recoupling in 2D experimental protocols

Consider an arbitrary recoupling sequence. Each of its *first*-order average Hamiltonian terms of interaction $\Lambda$ contributing to Eq. (13) is denoted $\overline{H}^{\Lambda}_{lm\lambda\mu}$ and associated with a quartet of spatial and spin quantum numbers ($l$, $m$, $\lambda$, $\mu$). To *second*-order AHT (Eq. (14)) a set of "cross-terms" are recoupled, each corresponding to a pair of quantum number quartets $\{(l_2m_2\lambda_2\mu_2), (l_1m_1\lambda_1\mu_1)\}$, associated with the Hamiltonian $\overline{H}^{\Lambda_2\times\Lambda_1}_{\substack{l_2m_2\lambda_2\mu_2\\ l_1m_1\lambda_1\mu_1}}$. The expressions of these Hamiltonians for symmetry-based pulse sequences are defined in [20,21,33].

To keep the notation in this Appendix consistent with the main text and most of the literature, we denote the evolution interval of a 2D NMR experiment by $t_1$, although we otherwise carefully distinguish between time-*points*, denoted $t$, and time *intervals*, denoted $\tau$. It is desirable to obtain purely absorptive peak-shapes combined with arbitrary spectral windows in both dimensions of the spectrum. However, these goals are often not simultaneously achievable in powdered solids when incorporating recoupling sequences into 2D protocols, such as that of Fig. 1C. In general, the 2D spectral amplitudes will be modulated because the starting point of the reconversion sequence is shifted (i.e., the rotor position) as $t_1$ is incremented, which leads to spinning sidebands (that cannot be suppressed by fast spinning) in the $\omega_1$ dimension unless $\Delta t_1 = \tau_r$ [3]. This *rotor-encoding* of the 2D amplitudes [21] may be avoided if the recoupling sequence is $\gamma$-encoded, meaning that each spin component $\mu$ of the Hamiltonian is only associated with *one* spatial component $m$ [21,60]. Hence, $\gamma$-encoded sequences allow using arbitrary incrementation in $t_1$, implying that $\Delta t_1$ may be chosen independently of the spinning frequency.

In the following, we first recapitulate the strategy presented earlier in [21,31,61] to circumvent rotor-encoding for first-order recoupling sequences. Next, these arguments are extended to second-order recoupling sequences. We discuss the restrictions imposed on the second-order average Hamiltonian of a general symmetry-based recoupling sequence (not necessarily effecting 3Q recoupling) when it is incorporated into a 2D correlation experiment as shown in Fig. 1C. Note that none of these restrictions apply to the 1Q–1Q correlation experiment of Fig. 1B as the MQC excitation and reconversion occurs *after* the $t_1$ interval.

### A.1. First-order recoupling sequences

Consider a rotor-synchronized $CN^{\nu}_{n}$ or $RN^{\nu}_{n}$ pulse sequence, having an overall RF phase $\Phi^0$ and starting at time point $t^0$. Assume that this sequence recouples a term $\overline{H}^{\Lambda}_{lm\lambda\mu}$ with quantum numbers ($l$, $m$, $\lambda$, $\mu$) to first-order average Hamiltonian theory. The term depends on $\Phi^0$ and $t^0$ as follows:

$$\overline{H}^{\Lambda}_{lm\lambda\mu}(t^0,\Phi^0) = \overline{H}^{\Lambda}_{lm\lambda\mu}(0,0)\exp\{-\mathrm{i}(\mu\Phi^0 - m\omega_r t^0)\}. \tag{A.1}$$

If the ratio $m/\mu$ is *equal* for *all* recoupled *terms* in the first-order average Hamiltonian, and additionally $\mu \neq 0$, their dependence on the starting time point $t^0$ of the pulse sequence can be canceled by choosing the overall RF phase $\Phi^0$ according to [21,31,61]

$$\Phi^0 = \frac{m}{\mu}\omega_r t^0. \tag{A.2}$$

By definition, all $\gamma$-encoded pulse sequences fulfill this condition.

Next, assume the pulse sequence (Fig. 1C) involves excitation and reconversion of multiple quantum coherences. The excitation sequence starts at time point $t^0_{\mathrm{exc}}$ and lasts for a time interval $\tau_{\mathrm{exc}}$, followed by an evolution interval $t_1$. The subsequent reconversion sequence starts at time point $t^0_{\mathrm{rec}} = t^0_{\mathrm{exc}} + \tau_{\mathrm{exc}} + t_1$. Then the RF phase $\Phi_{\mathrm{rec}}$ of the reconversion sequence should be adjusted according to Eq. (A.2)

$$\Phi_{\mathrm{rec}} = \Phi^0_{\mathrm{rec}} + \frac{m}{\mu}\omega_r(t^0_{\mathrm{rec}} - t^0_{\mathrm{exc}}) = \Phi^0_{\mathrm{rec}} + \frac{m}{\mu}\omega_r(\tau_{\mathrm{exc}} + t_1), \tag{A.3}$$

where $\Phi^0_{\mathrm{rec}}$ is an additional phase shift of the reconversion sequence. If $\tau_{\mathrm{exc}}$ is equal to an integer number of rotational periods, Eq. (A.3) is simplified to

$$\Phi_{\mathrm{rec}}(t_1) = \Phi^0_{\mathrm{rec}} + \frac{m}{\mu}\omega_r t_1. \tag{A.4}$$

Provided that the reconversion block implements this $t_1$-dependent phase-shift in a 2D experiment, an arbitrary incrementation in $t_1$ may be used.

### A.2. Second-order recoupling sequences

The previous discussion may readily be extended to second-order recoupling schemes. Again, consider a $CN^v_n$ or $RN^v_n$ pulse scheme, having an overall RF phase $\Phi^0$ and starting at time point $t^0$. Assume that it recouples a term $\overline{H}^{\Lambda_2\times\Lambda_1}_{\substack{l_2 m_2 \lambda_2 \mu_2 \\ l_1 m_1 \lambda_1 \mu_1}}$ with quantum numbers $\{(l_2 m_2\ \lambda_2\mu_2), (l_1 m_1 \lambda_1 \mu_1)\}$ to second-order average Hamiltonian theory. This term depends in the following way on $\Phi^0$ and $t^0$:

$$\overline{H}^{\Lambda_2\times\Lambda_1}_{\substack{l_2 m_2 \lambda_2 \mu_2 \\ l_1 m_1 \lambda_1 \mu_1}}(t^0,\Phi^0) = \overline{H}^{\Lambda_2\times\Lambda_1}_{\substack{l_2 m_2 \lambda_2 \mu_2 \\ l_1 m_1 \lambda_1 \mu_1}}(0,0)\exp\{-\mathrm{i}((\mu_2+\mu_1)\Phi^0 - (m_2+m_1)\omega_r t^0)\}. \tag{A.5}$$

A second-order recoupling sequence is $\gamma$-encoded if the ratio $(m_2+m_1)/(\mu_2+\mu_1)$ is equal for all recoupled second-order terms. if $\mu_2+\mu_1 \neq 0$, the dependence on the starting time point $t^0$ may then be removed, by choosing the overall rf phase $\Phi^0$ according to the phase-time relationship. If $\mu_2+\mu_1 \neq 0$, the dependence on the starting time point $t^0$ may then be removed, by choosing the overall RF phase $\Phi^0$ according to the phase-time relationship

$$\Phi^0 = \frac{m_2+m_1}{\mu_2+\mu_1}\omega_r t^0. \tag{A.6}$$

If we consider the pulse scheme of Fig. 1C, incorporating a $\gamma$-encoded recoupling sequence and implemented with excitation and reconversion intervals equal to an integer number of rotational periods, the RF phase $\Phi_{\mathrm{rec}}$ of the reconversion block has to be adjusted as

$$\Phi_{\mathrm{rec}}(t_1) = \Phi^0_{\mathrm{rec}} + \frac{m_2+m_1}{\mu_2+\mu_1}\omega_r t_1 \tag{A.7}$$

analogously to Eq. (A.4).

However, $\gamma$-encoded second-order recoupling sequences are in general more difficult to engineer than their first-order counterparts, due to the larger number of second-order terms contributing to the second-order average Hamiltonian. We therefore define that a pulse sequence is $\gamma$-encoded with resepect to a certain spin order $|\mu_2+\mu_1|$ if the ratio $(m_2+m_1)/\mu_2+\mu_1$ is the same for all terms order $|\mu_2+\mu_1|$. For these terms, Eqs. (A.5) and (A.7) are still valid. The sequence $(\mathrm{R}18^7_3)3^1$ is $\gamma$-encoded with respect to spin order 3, as all its recoupled 3Q terms (given in Table III of Ref. [20]) fulfill $(m_2+m_1)/(\mu_2+\mu_1) = 1/3$, explaining the choice of $t_1$-dependent phase incrementation $\frac{1}{3}\Delta t_1 \omega_r$ in our experiments.

## References


[1] M. Munowitz, A. Pines, Principles and applications of multiple-quantum NMR, Adv. Chem. Phys. 66 (1987) 1–152.
[2] G.P. Drobny, J.R. Long, T. Karlsson, W. Shaw, J. Popham, N. Oyler, P. Bower, J. Stringer, D. Gregory, M. Mehta, P.S. Stayton, Structural studies of biomaterials using double-quantum solid-state NMR spectroscopy, Ann. Rev. Phys. Chem. 54 (2003) 531–571.
[3] I. Schnell, Dipolar recoupling in fast-MAS solid-state NMR spectroscopy, Prog. NMR Spectrosc. 45 (2004) 145–207.
[4] D. Suter, S.B. Liu, J. Baum, A. Pines, Multiple quantum NMR excitation with a one-quantum Hamiltonian, Chem. Phys. 114 (1987) 103–109.
[5] Y.S. Yen, A. Pines, Multiple-quantum NMR in solids, J. Chem. Phys. 78 (1983) 3579–3582.
[6] J. Baum, M. Munowitz, A.N. Garroway, A. Pines, Multiple-quantum dynamics in solid state NMR, J. Chem. Phys. 83 (1985) 2015–2025.
[7] M. Munowitz, M. Mehring, Liouville space revisited: excitation and relaxation of multiple-quantum nuclear spin coherence in dipolar systems, Solid State Commun. 64 (1987) 605–608.
[8] Y. Ba, W.S. Veeman, On multiple quantum NMR of coupled spins in solids, Isr. J. Chem. 32 (1992) 173–178.
[9] B.E. Scruggs, K.K. Gleason, Computer-simulation of the multiple-quantum dynamics of one-, two- and three-dimensional spin distributions, Chem. Phys. 166 (1992) 367–378.
[10] G. Cho, J.P. Yesinowski, Multiple-quantum NMR dynamics in the quasi-one-dimensional distribution of protons in hydroxyapatite, Chem. Phys. Lett. 205 (1993) 1–5.
[11] R. Tycko, Selection rules for multiple quantum NMR experiments in solids: derivation from time-reversal symmetry and comparison with simulations and $^{13}$C NMR experiments, J. Magn. Reson. 139 (1999) 302–307.
[12] M. Munowitz, Exact simulation of multiple-quantum dynamics in solid-state NMR: implications for spin counting, Mol. Phys. 71 (1990) 959–978.
[13] E.B. Feldman, S. Lacelle, Multiple quantum nuclear magnetic resonance in one-dimensional quantum spin chains, J. Chem. Phys. 107 (1997) 7067–7084.
[14] S. Doronin, E.B. Feldman, S. Lacelle, Multiple-quantum nuclear magnetic resonance spin dynamics in disordered rigid chains and rings, J. Chem. Phys. 117 (2002) 9646–9650.
[15] S. Dusold, A. Sebald, Dipolar recoupling under magic-angle-spinning conditions, Ann. Rep. NMR Spectrosc. 41 (2000) 185–264.
[16] C.E Hughes, J. Schmedt auf der Günne, M.H. Levitt, A test for the number of coupled spins $I = 1/2$ in solids. Zero-quantum recoupling of multiple-quantum coherences, ChemPhysChem 4 (2003) 457–465.
[17] M. Edén, A. Brinkmann, H. Luthman, L. Eriksson, M.H. Levitt, Determination of molecular geometry by high-order multiple-quantum evolution in solid-state NMR, J. Magn. Reson. 144 (2000) 266–279.
[18] M. Schneider, L. Gasper, D.E. Demco, B. Blümich, Residual dipolar couplings by $^1$H dipolar-encoded longitudinal magnetization, double- and triple-quantum nuclear magnetic resonance in cross-linked elastomers, J. Chem. Phys. 111 (1999) 402–415.
[19] M. Edén, Order-selective multiple-quantum excitation in magic-angle spinning NMR: creating triple-quantum coherences with a trilinear Hamiltonian, Chem. Phys. Lett. 366 (2002) 469–476.
[20] A. Brinkmann, M. Edén, Second order average Hamiltonian theory of symmetry-based pulse schemes in the nuclear magnetic resonance of rotating solids: application to triple-quantum dipolar recoupling, J. Chem. Phys. 120 (2004) 11726–11744.
[21] M.H. Levitt, Symmetry-based pulse sequences in magic-angle spinning solid state NMR, Encyclopedia of NMR vol 19: Advances in NMR 2002, pp. 165–196.

[22] U. Haeberlen, High Resolution NMR in Solids. Selective Averaging, Academic Press, New York, 1976.
[23] M. Mehring, Principles of High Resolution NMR in Solids, Springer, Berlin, 1983.
[24] W.S. Warren, D.P. Weitekamp, A. Pines, Theory of selective excitation of multiple-quantum transitions, J. Chem. Phys. 73 (1980) 2084–2099.
[25] M. Ernst, S. Bush, A.C. Kolbert, A. Pines, Second-order recoupling of chemical-shielding and dipolar-coupling tensors under spin decoupling in solid-state NMR, J. Chem. Phys. 105 (1996) 3387–3397.
[26] S. Macura, R.R. Ernst, Elucidation of cross relaxation in liquids by two-dimensional NMR spectroscopy, Mol. Phys. 41 (1980) 95–117.
[27] A. Bax, R. Freeman, S.P. Kempsell, Natural abundance $^{13}C$–$^{13}C$ coupling observed via double-quantum coherence, J. Am. Chem. Soc. 102 (1980) 4849–4851.
[28] H. Geen, J. Gottwald, R. Graf, R. Graf, I. Schnell, H.W. Spiess, J.J. Titman, Elucidation of dipolar coupling networks under magic-angle-spinning, J. Magn. Reson. 125 (1997) 224–227.
[29] M. Hohwy, C.M. Rienstra, C.P. Jaroniec, R.G. Griffin, Fivefold symmetric homonuclear dipolar recoupling in rotating solids: application to double quantum spectroscopy, J. Chem. Phys. 110 (1999) 7983–7992.
[30] M. Hong, Solid-state dipolar INADEQUATE NMR spectroscopy with a large double-quantum spectral width, J. Magn. Reson. 136 (1999) 86–91.
[31] A. Brinkmann, M. Edén, M.H. Levitt, Synchronous helical pulse sequences in magic-angle-spinning NMR. Double quantum spectroscopy of recoupled multiple-spin systems, J. Chem. Phys. 112 (2000) 8539–8554.
[32] M. Carravetta, M. Edén, X. Zhao, A. Brinkmann, M.H. Levitt, Symmetry principles for the design of radiofrequency pulse sequences in the nuclear magnetic resonance of rotating solids, Chem. Phys. Lett. 321 (2000) 205–215.
[33] A. Brinkmann, M.H. Levitt, Symmetry principles in the nuclear magnetic resonance of spinning solids: heteronuclear recoupling by generalized Hartmann–Hahn sequences, J. Chem. Phys. 115 (2001) 357–384.
[34] M. Edén, Enhanced symmetry-based dipolar recoupling in solid-state NMR, Chem. Phys. Lett. 378 (2003) 55–64.
[35] A.E. Bennett, C.M. Rienstra, M. Auger, K.V. Lakshmi, R.G. Griffin, Heteronuclear decoupling in rotating solids, J. Chem. Phys. 103 (1995) 6951–6958.
[36] M. Carravetta, M. Edén, O.G. Johannessen, H. Luthman, P.J.E. Verdegem, J. Lugtenburg, A. Sebald, M.H. Levitt, Estimation of carbon–carbon bond lengths and medium-range internuclear distances by solid-state nuclear magnetic resonance, J. Am. Chem. Soc. 123 (2001) 10628–10638.
[37] R.R. Ernst, G. Bodenhausen, A. Wokaun, Principles of Nuclear Magnetic Resonance in One and Two Dimensions, Clarendon Press, Oxford, 1987.
[38] B.-Q. Sun, P.R. Costa, D. Kocisko, P.T. Lansbury, R.G. Griffin, Internuclear distance measurements in solid state nuclear magnetic resonance: dipolar recoupling via rotor synchronized spin locking, J. Chem. Phys. 102 (1995) 702–707.
[39] U. Friedrich, I. Schnell, D.E. Demco, H.W. Spiess, Triple-quantum NMR spectroscopy in dipolar solids, Chem. Phys. Lett. 285 (1998) 49–58.
[40] D.A. Varshalovich, A.N. Moskalev, V.K. Khersonskii, Quantum Theory of Angular Momentum, World Scientific, Singapore, 1988.
[41] Y.K. Lee, N.D. Kurur, M. Helmle, O.G. Johannessen, N.C. Nielsen, M.H. Levitt, Efficient dipolar recoupling in the NMR of rotating solids. A sevenfold symmetric radiofrequency pulse sequence, Chem. Phys. Lett. 242 (1995) 304–309.
[42] W. Magnus, On the exponential solution of differential equations for a linear operator, Com. Pure. Appl. Math. 7 (1954) 649–673.
[43] M. Hohwy, H.J. Jakobsen, M. Edén, M.H. Levitt, N.C. Nielsen, Broadband dipolar recoupling in the nuclear magnetic resonance of rotating solids: a compensated C7 pulse sequence, J. Chem. Phys. 108 (1998) 2686–2694.
[44] M. Edén, M.H. Levitt, Pulse sequence symmetries in the nuclear magnetic resonance of spinning solids: application to heteronuclear decoupling, J. Chem. Phys. 111 (1999) 1511–1519.
[45] J. Jeener, Superoperators in magnetic resonance, Adv. Magn. Reson. 10 (1982) 1.
[46] S. Caldarelli, L. Emsley, Intrinsic asymmetry in multidimensional solid-state NMR correlation spectra, J. Magn. Reson. 130 (1998) 233–237.
[47] R. Tycko, G. Dabbagh, Double-quantum filtering in magic-angle-spinning NMR spectroscopy: an approach to spectral simplification and molecular structure determination, J. Am. Chem. Soc. 113 (1991) 9444–9448.
[48] M. Feike, D.E. Demco, R. Graf, J. Gottwald, S. Hafner, H.W. Spiess, Broadband multiple-quantum NMR spectroscopy, J. Magn. Reson. A 122 (1996) 214–221.
[49] O.W. Sørensen, J. Magn. Reson. 86 (1990) 435–440.
[50] M. Edén, M.H. Levitt, Excitation of carbon-13 triple quantum coherence in magic-angle-spinning NMR, Chem. Phys. Lett. 293 (1998) 173–179.
[51] M. Carravetta, J. Schmedt auf der Günne, M.H. Levitt, Enhanced triple-quantum excitation in $^{13}C$ magic-angle spinning NMR, J. Magn. Reson. 162 (2003) 443–453.
[52] N.A. Oyler, R. Tycko, Multiple quantum $^{13}C$ spectroscopy under high-speed magic-angle spinning, J. Phys. Chem. B 106 (2002) 8382–8389.
[53] Y. Ishii, J. Ashida, T. Terao, $^{13}C$–$^{1}H$ dipolar recoupling dynamics in $^{13}C$ multiple-pulse solid-state NMR, Chem. Phys. Lett. 246 (1995) 439–445.
[54] A.E. Bennett, C.M. Rienstra, J.M. Griffiths, W. Zen, P.T. Lansbury Jr., R.G. Griffin, Homonuclear radio frequency-driven recoupling in rotating solids, J. Chem. Phys. 108 (1998) 9463–9479.
[55] S. Wolfram, Mathematica, Wolfram Research, 2004.
[56] S.K. Zaremba, Good lattice points, discrepancy, and numerical integration, Ann. Mat. Pura. Appl. 4 (73) (1966) 293–317.
[57] H. Conroy, Molecular Schrödinger equation. VIII. A new method for the evaluation of multidimensional integrals, J. Chem. Phys. 47 (1967) 5307–5318.
[58] V.B. Cheng, H.H. Suzukawa, M. Wolfsberg, Investigations of a nonrandom numerical method for multidimensional integration, J. Chem. Phys. 59 (1973) 3992–3999.
[59] A. Mostad, H.M. Nissen, C. Rømming, Crystal structure of L-tyrosine, Acta Chem. Scand. 26 (1972) 3819–3833.
[60] N.C. Nielsen, H. Bildsøe, H.J. Jakobsen, M.H. Levitt, Double-quantum homonuclear rotary resonance: efficient dipolar recovery in magic-angle-spinning nuclear magnetic resonance, J. Chem. Phys. 101 (1994) 1805–1812.
[61] P.E. Kristiansen, D.J. Mitchell, J.N.S. Evans, Double-quantum dipolar recoupling at high magic-angle spinning rates, J. Magn. Reson. 157 (2002) 253–266.